

Supplementary Materials for

Battery-free, wireless sensors for full-body pressure and temperature mapping

Seungyong Han, Jeonghyun Kim, Sang Min Won, Yinji Ma, Daeshik Kang, Zhaoqian Xie, Kyu-Tae Lee, Ha Uk Chung, Anthony Banks, Seunghwan Min, Seung Yun Heo, Charles R. Davies, Jung Woo Lee, Chi-Hwan Lee, Bong Hoon Kim, Kan Li, Yadong Zhou, Chen Wei, Xue Feng, Yonggang Huang,* John A. Rogers*

*Corresponding author. Email: y-huang@northwestern.edu (Y.H.); jrogers@northwestern.edu (J.A.R.)

Published 4 April 2018, *Sci. Transl. Med.* **10**, eaan4950 (2018)
DOI: 10.1126/scitranslmed.aan4950

The PDF file includes:

Materials and Methods

Fig. S1. Process for calibrating the temperature sensors.

Fig. S2. Operation of calibrated wireless temperature sensors during rapid changes in temperature, with comparison to results obtained using an IR camera.

Fig. S3. Thermal FEA results as a function of thickness of the bottom PDMS layer.

Fig. S4. Photograph and structure schematic of silicon membrane, with comparison of pressure sensors with different shapes using FEA.

Fig. S5. Mechanism of strain generation in the sensor under uniform normal pressure.

Fig. S6. Effect of bending on the pressure sensor.

Fig. S7. Characterization of the boron-doped silicon pressure module.

Fig. S8. Screen view of temperature monitoring with a smartphone application in real time.

Fig. S9. Measurements of the effect of orientation under three power settings and representative positions.

Fig. S10. Measurements of operating distance for sensors placed at various locations inside each antenna with different power levels.

Fig. S11. Distributions of the magnetic field along the vertical direction for constant power (12 W) and different antenna sizes.

Fig. S12. Simulation of field strength of different antenna sizes and multiplexed operation.

Fig. S13. Embedded antenna setup for sleep studies at Carle Hospital.
Fig. S14. Results of sleep studies conducted with arrays of temperature sensors on the front of the body.
Fig. S15. Results of sleep studies conducted with arrays of temperature sensors on the back of the body.
Fig. S16. Color heat maps of the entire body constructed from temperature data collected using NFC sensors.
Fig. S17. Results of the sensors' lifetime during 3 days of continuous wear.
Fig. S18. Results of wirelessly recorded data obtained while lying at a supine angle of 30°.
Fig. S19. Graphs of pressure measurements in a hospital bed while lying at a supine angle of 0° (data with individual sensor).
Fig. S20. Graphs of pressure measurements obtained in a hospital bed while lying at a supine angle of 30° (data with individual sensor).
Fig. S21. Graphs of pressure measurements obtained in a hospital bed while lying at a supine angle of 60° (data with individual sensor).
Fig. S22. Summary of comparative studies of temperature measurements in a clinical sleep laboratory: first night.
Fig. S23. Summary of the experimental setup and data collected in comparative studies of temperature measurements in a clinical sleep laboratory: second night.
Fig. S24. Demonstration of a gate-type reader system and antenna.
Fig. S25. Strain distributions at the silicon layer induced by local pressure.
Fig. S26. Measurements of response time obtained using a vibrating actuator stage and a function generator.
Fig. S27. Mechanical response of an encapsulated sensor on a phantom skin under stretching, bending, and twisting.
Legends for movies S1 and S2

Other Supplementary Material for this manuscript includes the following:

(available at

www.sciencetranslationalmedicine.org/cgi/content/full/10/435/eaan4950/DC1)

Movie S1 (.avi format). Recordings from a single sensor captured using NFC between an epidermal device and a smartphone through a prosthetic.

Movie S2 (.avi format). Recordings from four sensors simultaneously using a large-scale (800 mm × 580 mm × 400 mm) RF antenna through a prosthetic.

Materials and Methods

Procedure for fabricating temperature and pressure sensors.

1. Cut a commercial Cu film to the size of a glass slide (76 x 51 mm, microscope slide).
2. Spin coat with polyimide (PI, poly (pyromellitic dianhydride-co-4,4' -oxydianiline), amic acid solution, Sigma-Aldrich) at 3,000 rpm for 30 s.
3. Bake at 110 °C for 30 s.
4. Bake at 150 °C for 5 min.
5. Bake at 250 °C under vacuum for 1 hr.
6. Spin coat a glass slide with PDMS (Sylgard 184, 10:1, 1000 rpm, 30 s), to a thickness of 25 µm.
7. Bake at 110 °C for 10 min.
8. Affix the Cu/PI bilayer onto the PDMS-coated glass slide.
9. Photolithographically pattern (365 nm wavelength; iron oxide mask; Mark Suss MJB3) a layer of photoresist (PR; Clariant AZ4620, 3000 rpm, 30s;) to define the geometry of the loop antenna. Develop in aqueous base developer. (AZ 400K, diluted 2:1)
10. Etch Cu with Cu etchant.
11. Remove PR with acetone. Rinse with IPA.
12. Spin coat with PI at 3,000 rpm for 30 s.
13. Bake at 110 °C for 30 s.
14. Bake at 150 °C for 5 min.
15. Bake at 250 °C under vacuum for 1 hr.
16. Pattern PR (AZ4620) to define via holes.

17. Reactive ion etch (RIE; March CS-1701, 200 mTorr, 20 sccm O₂, 150 W, 15 min) to open the vias.
18. Remove PR with acetone. Rinse with IPA.
19. Deposit 1 μm Cu by electron beam evaporation.
20. Pattern PR (AZ4620) to define the bridge interconnect and the electrodes.
21. Etch Cu with Cu etchant.
22. Remove PR with acetone. Rinse with IPA.
23. Spin coat with PI at 3,000 rpm for 30 s.
24. Bake at 110 °C for 30 s.
25. Bake at 150 °C for 5 min.
26. Anneal at 250 °C under vacuum for 1 hr.
27. Deposit 100 nm SiO₂ by electron beam evaporation.
28. Pattern PR (AZ4620) for perimeter of NFC coil structure.
29. Reactive ion etch (RIE; March CS-1701, 200 mTorr, 20 sccm O₂, 180 W, 50 min) to remove the SiO₂
30. Prepare a glass slide with PMMA coating. (3000 rpm, 30 s, thickness; 10μm)
31. Bake at 180 °C for 3 min.
32. Spin coat the glass slide with PDMS. (Sylgard 184, 30:1, 1000 rpm, 30 s, thickness; 50 μm)
33. Bake at 110 °C for 15 min.
34. Transfer device with water-soluble tape to a glass slide coated with PMMA and PDMS.
31. Apply FLUX WORTHINGTON; 334436) on the electrodes.

32. Solder the NFC chip, resistor, and silicon membrane pressure sensor to appropriate locations.
33. Encapsulate by spin-coating with PDMS (Sylgard 184, 30:1, 300 rpm, 30 s).
34. Cut through the top and bottom layer of PDMS around the perimeter of the device.
35. Add adhesive tape on the bottom of the device by oxygen-plasma treatment.

Fabrication procedure of p+ doping silicon based pressure module.

1. Clean a silicon on insulator (SOI) wafer by immersion in concentrated HF for 10 s, in piranha solution (a mixture of sulfuric acid (H_2SO_4) and hydrogen peroxide (H_2O_2), 3:1 ratio) for 3 min, and then in concentrated HF for 10 s.
2. Perform solid state doping of the silicon by exposure to a boron source at 1000°C for 25 min.
3. Clean the wafer again using the process of step 1.
4. Photolithographically pattern holes in a layer of photoresist (PR S1805, 3000 rpm, 30 s) and then develop in aqueous base developer. (MIF 917).
5. Remove the exposed silicon by RIE (50 mTorr, 40 sccm SF_6 , 100W, 1 min).
6. Etch the SiO_2 layer by immersion in concentrated HF for 30 min.

Substrate preparation

7. Spin coat a layer of PDMS (Sylgard 184, 10:1, 3000 rpm, 30 s) on a glass slide.
8. Attach a PET film (thickness; $25\ \mu\text{m}$) on PDMS.
9. Spin coat a layer of photodefinable epoxy. (SU-8 2007, Microchem Corp, 3000 rpm, 30 s, thickness; $1.5\ \mu\text{m}$)
10. Bake at 65°C for 1 min.

11. Bake at 95°C for 2 min.

Transfer printing

12. Retrieve the top Si layer onto the surface of a PDMS stamp.

13. Transfer print the Si layer onto a prepared PET film.

14. Bake at 95°C for 2 min.

15. Remove PR with acetone. Rinse with IPA.

Silicon isolation

16. Photolithographically pattern a layer of PR (5214, 3000 rpm, 30 s) and develop in MIF 917. This pattern defines the spiral shape.

17. Remove the exposed silicon by RIE (50 mTorr, 40 sccm SF₆, 100 W, 1 min).

18. Remove PR with acetone. Rinse with IPA.

19. Photolithographically pattern a layer of PR (nLOF 2070, 2500 rpm, 30s) and develop in MIF 917. This pattern defines the contact electrodes.

20. Etch residual oxide by immersion in BOE (NH₄F : HF = 10 : 1) for 15 s.

21. Deposit 13/150 nm of Cr/Au by electron beam evaporation.

22. Perform lift-off by immersion in acetone.

23. Spin coat PI at 3000 rpm and 30 s.

24. Bak at 150 °C for 1 hr.

25. Photolithographically pattern a layer of PR. (electrodes) MORE DETAILS?

26. Etch PI with RIE (200 mTorr, 20 sccm O₂, 150 W, 15 min).

27. Remove PR with acetone. Rinse with IPA.

Temperature measurement and calibrations.

Figure S1 shows the results of tests to define calibration factors for the output of a wireless sensor. As in fig. S1A, the tests involved placing a sensor on an anodized Al plate on a hotplate. Measurements from the sensor and readings from an IR camera were collected as the temperature changed from 25°C to 50°C. Each sensor required a slightly different calibration factor, defined by a single multiplier that converts the wireless reading to a value that matched that from the IR camera, as shown in fig. S1D.

Pressure measurement and calibrations.

Detailed characterization of the pressure sensor appears in fig. S7. A commercial force gauge (Mark-10, Resolution: $\pm 0.25\%$) fixed on a Z-stage controller with a 6.6 mm diameter, circle-shaped tip provides a controlled source of pressure as shown in inset image of fig. S7A. As the tip delivers force uniformly across the pressure sensor, a fractional change in resistance of the silicon spiral structure ($\Delta R/R$) occurs in a systematic manner.

The stability of operation is important to consider. Experimental studies defined the linearity of the response, the response speed and the extent of hysteresis (fig. S7B). Data in fig. S7A summarizes the results, which showed expected changes in resistance with pressure, time and cycles of loading/unloading. Changes in resistance associated with changes in temperature or bending radius are important to understand. Figure S7C presents the changes in resistance associated with temperature changes between 25 and 50 °C. For a range relevant to skin temperatures (red box), the resistance change is 0.5%, which corresponds to ~2 kPa pressure on a flat surface. Figure S7D summarizes changes in resistance as a function of bending radius. For most cases of relevance to mounting on the body (red box), the bending induced change in

resistance is 0.8%, which corresponds to ~ 3 kPa pressure on a flat surface. In practice, the temperature and degree of bending associated with mounting on the body set a baseline from which additional changes in resistance can be associated with pressure. Further, the temperature reading from the device can be used to compensate the pressure measurement for any effect of changes in temperature.

FEA for the thermal simulation of the encapsulated NFC device.

ABAQUS commercial software(47) was used to study the thermal response of the encapsulated NFC sensor on a forearm. The thickness of the encapsulated NFC device is much smaller than the encapsulation layer (PDMS) such that thermal properties of the encapsulated NFC device can be neglected. A transient FEA model of the encapsulation layer, as in fig. S3A, with an initial temperature of 23°C (the same as the ambient temperature), constant temperature boundary (the same as the forearm temperature, 34°C) at the bottom surface, and material properties of PDMS (thermal conductivity $k=0.15 \text{ W}\cdot\text{m}^{-1}\text{K}^{-1}$, heat capacity $c=1380 \text{ J}\cdot\text{kg}^{-1}\text{K}^{-1}$, and density $\rho=970 \text{ kg}\cdot\text{m}^{-3}$)(31), was established. Figure 2B gives the chip temperature versus time with a fixed $300 \mu\text{m}$ -thick top encapsulation layer and several bottom encapsulation layer thicknesses ($50, 100,$ and $200 \mu\text{m}$). Figure S3B-E shows the temperature distribution at the cross-section, the chip and the top surface at several times ($0, 0.1, 0.2, 0.5, 1$ and 5 sec) and bottom encapsulation layer thicknesses ($50, 100,$ and $200 \mu\text{m}$). As the thickness of the bottom encapsulation layer decreases, the steady-state temperature of the chip approaches that of the adjacent material ($33.89^{\circ}\text{C}, 33.81^{\circ}\text{C},$ and 33.66°C for $50, 100,$ and $200 \mu\text{m}$ -thick bottom encapsulation layers, respectively). In addition, a $50 \mu\text{m}$ -thick bottom encapsulation layer

reached the steady-state temperature faster than 100 μm - or 200 μm -thick bottom encapsulation layers.

Theory for the thermal response time of the encapsulated device.

As shown in fig. S3A, an encapsulated device involves layers of PDMS on the top and bottom surfaces. The in-plane dimensions of these layers are much larger than the thickness, such that the heat flux is mainly along the thickness direction, which can be represented by a one-dimensional heat transfer model

$$\frac{\partial T}{\partial t} - \alpha \frac{\partial^2 T}{\partial x^2} = 0 \quad (\text{Eq. S1})$$

where T is the temperature, $\alpha = k/\rho c$ is the thermal diffusivity of PDMS, and the coordinate x is along the thickness direction. The initial temperature of the PDMS is assumed to be the same as the ambient temperature

$$T|_{t=0} = T_{initial} \quad (\text{Eq. S2})$$

The skin provides a constant temperature T_{skin} at the bottom of the PDMS

$$T|_{x=0} = T_{skin} \quad (\text{Eq. S3})$$

Numerical analysis suggests that natural convection at the top surface of the PDMS has a negligible effect and can be approximated by a thermal isolation condition

$$\left. \frac{\partial T}{\partial x} \right|_{x=H_1+H_2} = 0 \quad (\text{Eq. S4})$$

Eqs. S1-S4 give the temperature of the encapsulated NFC device ($x = H_1$) versus time as

$$T_{sensor} = T_{skin} - (T_{skin} - T_{initial}) \sum_{n=1}^{\infty} \frac{4}{\pi(2n-1)} e^{-\frac{\pi^2(2n-1)^2 kt}{4\rho c(H_1+H_2)^2}} \sin\left[\frac{\pi(2n-1)H_1}{2(H_1+H_2)}\right] \quad (\text{Eq. S5})$$

with $T_{initial} = 23^\circ\text{C}$, $T_{skin} = 34^\circ\text{C}$, $H_2 = 300\mu\text{m}$, and material properties of PDMS as $k = 0.15 \text{ W}\cdot\text{m}^{-1}\text{K}^{-1}$, $c = 1380 \text{ J}\cdot\text{kg}^{-1}\text{K}^{-1}$, and $\rho = 970 \text{ kg}\cdot\text{m}^{-3}$. Figure 2B shows the temperature at the device ($H_1 = 300\mu\text{m}$) versus time with different H_1 ($50\mu\text{m}$, $100\mu\text{m}$ and $200\mu\text{m}$).

The sensor response time is defined by the time at which the sensor temperature change ($T_{sensor} - T_{initial}$) reaches 99% of the temperature difference between the skin and ambient temperature ($T_{skin} - T_{initial}$). The sensor response time is 1.6s, 2.4s and 4.0s for $H_1 = 50\mu\text{m}$, $100\mu\text{m}$, and $200\mu\text{m}$, respectively.

FEA of the pressure sensor under uniform pressure.

ABAQUS commercial software(47) was used to study the deformation and strain in the pressure sensor on skin under uniform pressure. Pressure sensors [200 nm-thick Si (elastic modulus 130 GPa and Poisson's ratio 0.27) with or without a 5 μm -thick PET layer (elastic modulus 4.5 GPa and Poisson's ratio 0.35)] were encapsulated by two PDMS layers (300 μm at top and 50 μm at bottom, elastic modulus 145 kPa and Poisson's ratio 0.5), which were then mounted on a skin substrate (elastic modulus 100-200 kPa and Poisson's ratio 0.5), and subjected to 10 kPa uniform pressure on the top surface as fig. S5A.

Figure S5B shows the strain distribution at the top, middle, and bottom of PET (through the thickness) for uniform pressure ($\sim 10 \text{ kPa}$) applied over the entire top surface (device and

skin). For the device with PET, the strain distributions at the top, middle and bottom are approximately the same, which suggests that the device (with PET) is mainly stretched, not bent. The strains (in the x -direction, fig. S5A) in fig. S5B are $\sim 10^{-5}$, which are much larger than the strain $\sim 10^{-6}$ that would result in PET (elastic modulus 4.5 GPa) when subjected directly to 10 kPa pressure. Instead, the pressure in the z -direction (fig. S5A) causes PDMS to expand in the x -direction due to the Poisson's effect. The expansion of PDMS is much larger than that of Si and PET because the modulus of PDMS is at least 4 orders of magnitude smaller than those of Si and PET. This expansion leads to stretching of silicon in the x -direction, thereby inducing a change in resistance due to pressure (rather than bending).

This conclusion is further validated by the strain distributions in fig. S5C-D for the hypothetical case of zero Poisson's ratio for PDMS. The strain in PET becomes much smaller than that of the reference case for non-zero Poisson's ratio of PDMS, which further confirms that the strain in the device with PET results mainly from stretching in the x -direction (due to the Poisson effect in PDMS). The strain distribution in the PET was insensitive to the Poisson's ratio of the skin. In conclusion, the mechanism of strain generation and resistance change under uniform pressure applied to a device on the skin is dominated by Poisson effects associated with the encapsulating PDMS and consequent stretching of the PET.

FEA for the mechanics simulation of the encapsulated device.

ABAQUS commercial software(47) was used to study the mechanics response of the encapsulated sensor on a phantom skin. The device (coil [1.2 μm -thick PI (elastic modulus 2.5 GPa and Poisson's ratio 0.34) / 5 μm -thick Cu (elastic modulus 119 GPa and Poisson's ratio 0.34) / 1.2 μm -thick PI], chip (100 μm -thick Si), serpentines (1.2 μm -thick PI / 2 μm -thick Cu / 1.2

μm -thick PI) and pressure sensor (5 μm -thick PET / 200 nm-thick Si)) is encapsulated by two PDMS layers (300 μm at top and 50 μm at bottom), which are then mounted on a phantom skin substrate (70 \times 50 \times 5 mm, PDMS with elastic modulus 145 kPa and Poisson's ratio 0.5) through a 50 μm -thick Scapa tape layer (elastic modulus \sim 17 kPa and Poisson's ratio 0.5). Figure S27 shows the FEA results of the deformed shape of the device under different types of external loads (stretching, bending and twisting). The stretching strain is defined as the percentage elongation of the phantom skin. The bending and twisting angles are defined as the relative in-plane and out-of-plane angles of rotation between the two ends of the phantom skin. The stretching strain, bending and twisting angles are 30 %, 180° and 90°, respectively, for the three types of external loads. The corresponding maximum strain in the copper layer, as shown in fig. S27B, is below the fracture limit (5%) under all the three loading conditions. For 30% stretching strain, the interfacial stresses between the encapsulated NFC device and phantom skin (fig. S27C) are within 20 kPa.(35) (threshold normal skin sensitivity)

FEA of the pressure sensor under bending.

Figure S6A shows the flat device and the skin substrate, where the geometric and material parameters are the same as those in supplementary materials (FEA of the pressure sensor under uniform pressure), subjected to 10 kPa pressure. To study the effect of bending, the skin (with the device) was bent to a curvature $1/50\text{mm}^{-1}$ without pressure (fig. S6B), and then 10kPa pressure was applied (fig. S6C). The strain in Si due to bending (fig. S6B) is much larger than that for the flat skin with pressure (fig. S6A) because Si is far from the neutral mechanical plane. For 10 kPa pressure applied to the bent state (fig. S6C), the induced strain distribution in

Si is very close to that for a flat state (fig. S6A) (~ 7% difference for the average strain). This result suggests that any initial bending has little effect on the additional strain due to pressure.

The influence of power and angle θ on operating range.

The magnetic flux ϕ through the sensor with an angle θ relative to the reader antenna is

$$\phi \approx A_{\text{sensor}} \cos \theta \frac{\mu_0 ab \sqrt{P/R}}{\pi \sqrt{a^2 + b^2 + Z^2}} \left[\frac{1}{a^2 + Z^2} + \frac{1}{b^2 + Z^2} \right] \quad (\text{Eq. S6})$$

where A_{sensor} is the area of the sensor, Z is the distance between sensor and reader antenna, a , b and P are the half width, half-length and power of the reader antenna, respectively, R is the impedance of the input port and μ_0 is the permeability of the vacuum. For a critical magnetic flux, Eq. S6 leads to the scaling law between the power and range in Eq. 3. For $a = 32$ cm and $b = 42.6$ cm, the range in the experiment is $Z = 12$ cm for power $P = 4$ W and $Z = 32$ cm for power $P = 12$ W, which satisfy approximately this scaling law. For points around the center and Z much larger than the a and b , the above formula gives $\phi \propto \cos \theta \sqrt{P} Z^{-3}$, the operation range is insensitive to angle change θ and the power P of the reader antenna. For example, the cosine term in this formula indeed gives 50% loss of magnetic flux at 60° compared to 0° . In order to maintain the same magnetic flux ϕ at a fixed power P , the operation range Z at $\theta = 60^\circ$ is only reduced to ~80% of that at $\theta = 0^\circ$, and this reduction (to ~80%) agrees well with the experiments. Similarly, in order to maintain the same ϕ at a fixed angle θ , the operation range at $P = 4$ W is only reduced to 91% of that at $P = 12$ W, and this reduction (to 91%) also agrees well with the experiments.

Supplementary figures

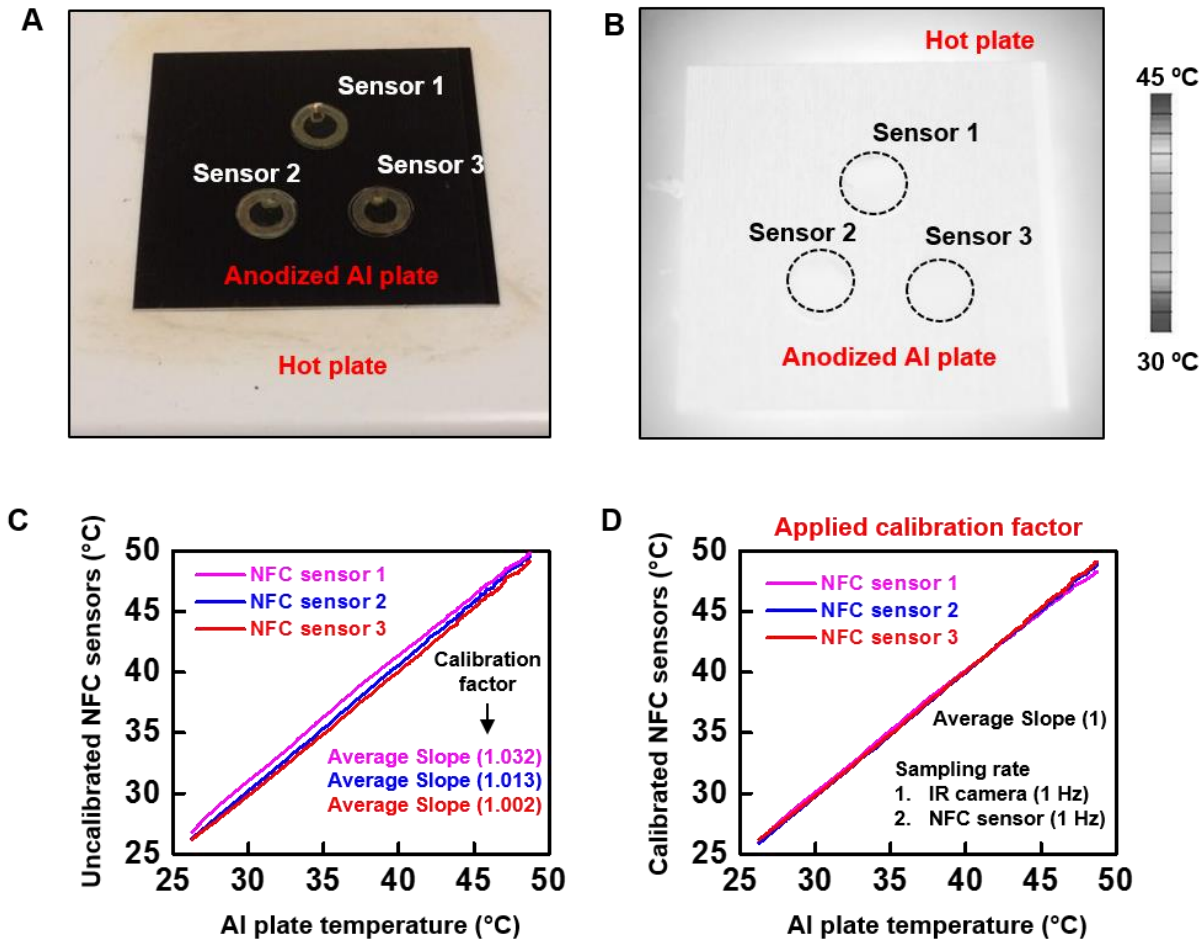


Fig. S1. Process for calibrating the temperature sensors. (A) Image of the calibration process. An anodized Al plate, heated from 25°C to 50°C on hot plate, served as a substrate support for each sensor. Comparisons involved temperature readings from an IR camera and each sensor, operated in a wireless mode. (B) IR camera image during calibration. This image shows that the anodized Al plate and the sensors have similar temperatures. (C) Measured temperatures from an uncalibrated sensor and the IR camera. (D) Temperatures after application of a calibration factor determined from the average slope of the measured data.

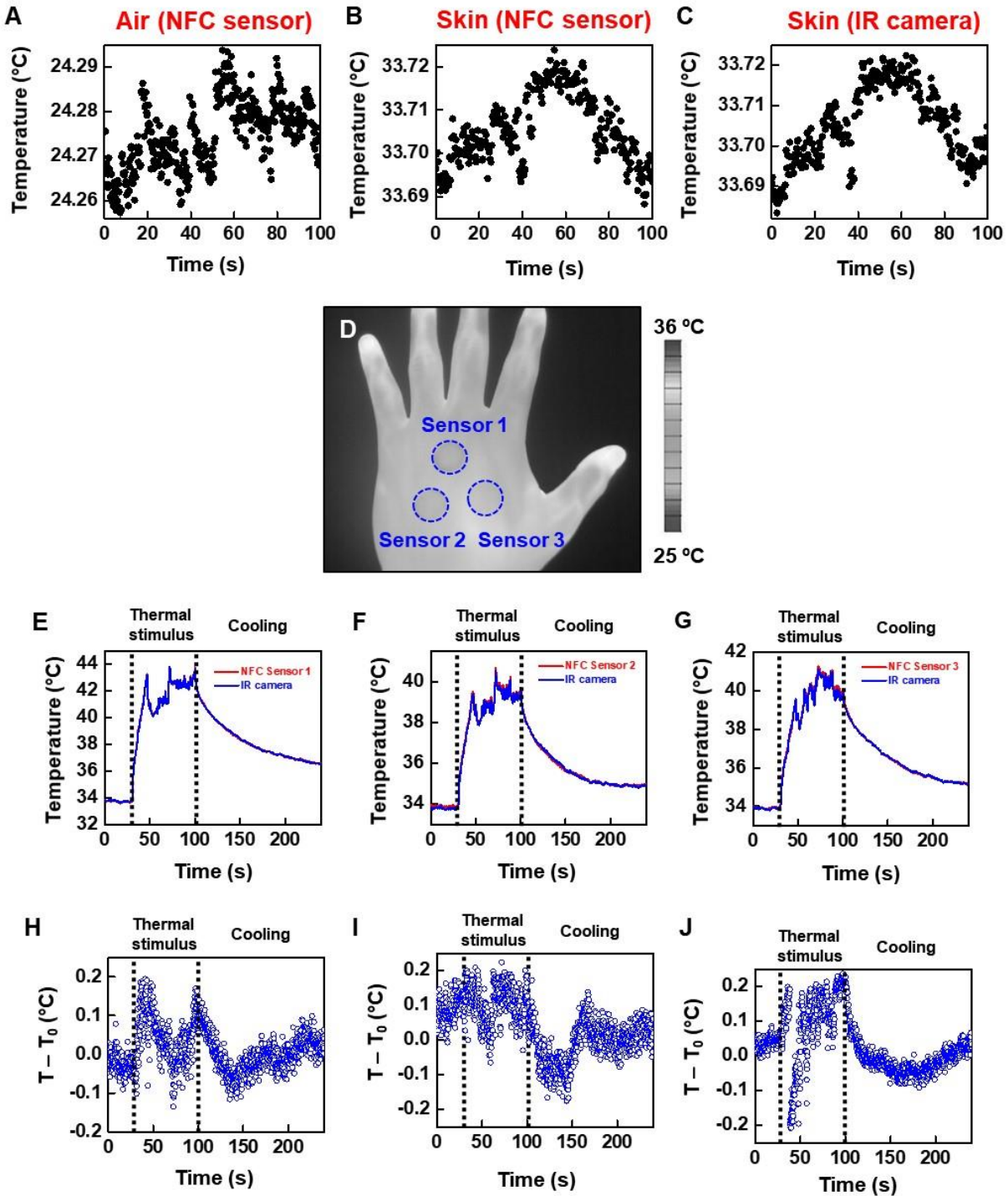


Fig. S2. Operation of calibrated wireless temperature sensors during rapid changes in temperature, with comparison to results obtained using an IR camera. (A) Measurements of temperature using an NFC sensor under temperature controlled conditions. **(B, C)** Measurements of temperature using an NFC sensor and an IR camera on the skin. The results show differences

less than 0.04 °C, thereby defining the precision of the measurement. **(D)** IR camera image of calibrated NFC temperature sensors mounted on healthy human skin. After 10~15 min of steady state operation, the sensors receive thermal stimulus from a stream of heated air (heat gun). Comparisons involve temperatures determined using the IR camera and the sensors. **(E-G)** The measurements yield similar temperatures **(G-J)** The differences between the NFC sensor (T) and IR camera (T_0) results indicate some differences, likely due to spatial non-uniformities in temperature, with a magnitude of $\sim 0.2^\circ\text{C}$.

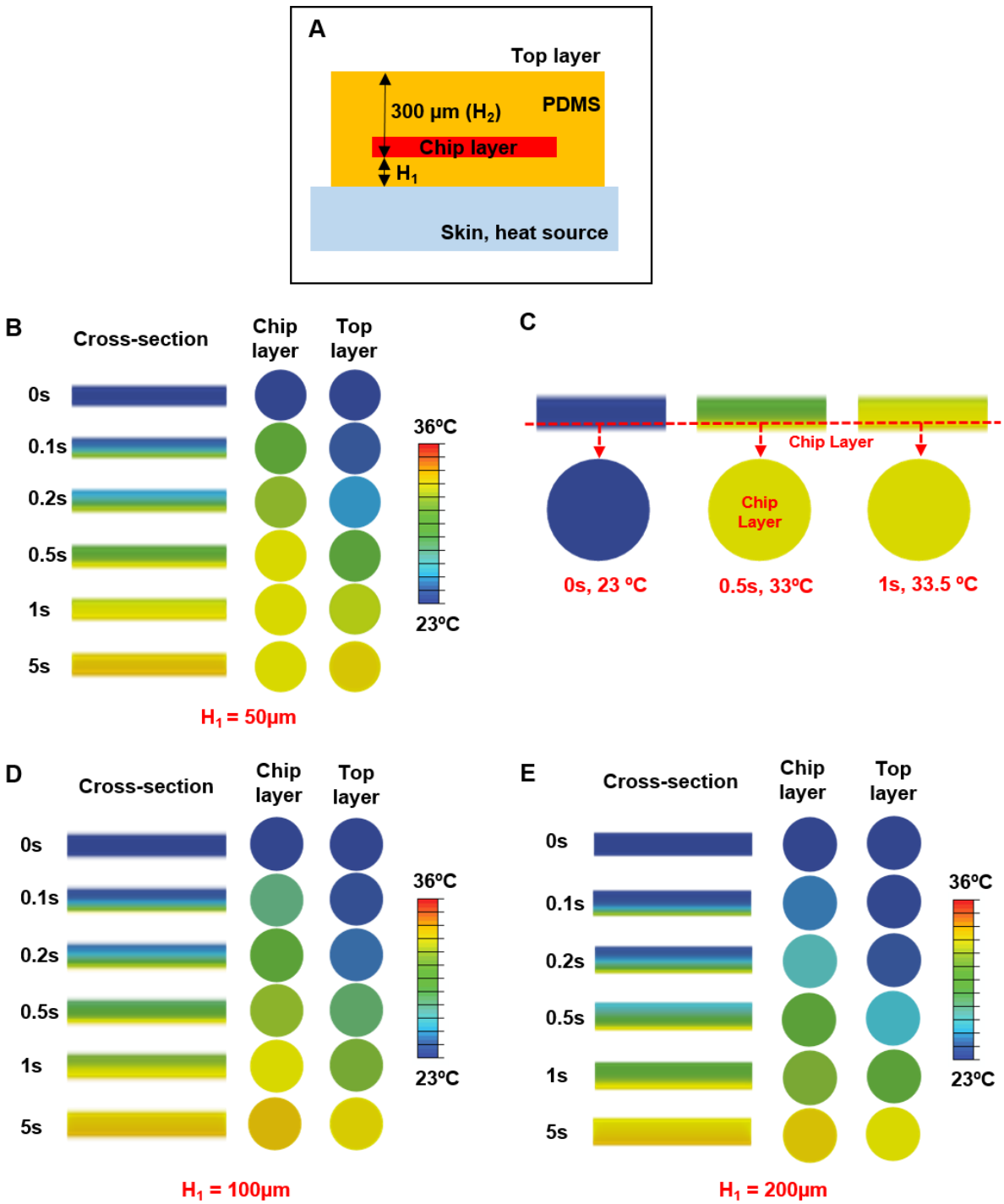


Fig. S3. Thermal FEA results as a function of thickness of the bottom PDMS layer. (A) Schematic illustration of the device structure used in the simulations. FEA results for temperatures at the NFC chip, the top surface, and for the characteristic thermal diffusion time

are shown for several thicknesses of the bottom PDMS (H_1); **(B-C)** 50 μm , **(D)** 100 μm , and **(E)** 200 μm . The top PDMS layer was 300 μm thickness as physical protection of the sensor.

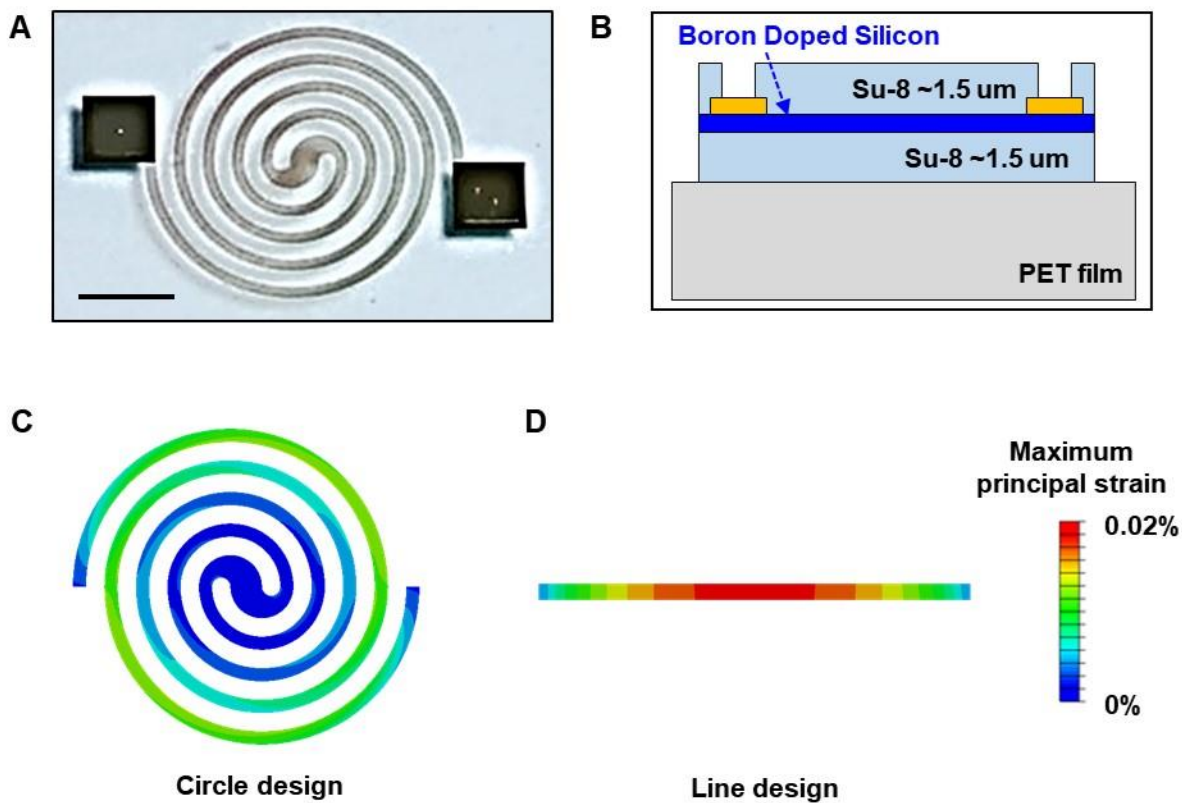


Fig. S4. Photograph and structure schematic of silicon membrane, with comparison of pressure sensors with different shapes using FEA. (A) Image of a spiral shaped silicon membrane on a PET film (Scale bar: 2 mm). (B) Schematic illustration of the structure of the pressure sensing module. Pressure-induced strain distributions in the Si layer for (C) circle design and (D) line design.

Fig. S5. Mechanism of strain generation in the sensor under uniform normal pressure. (A) Schematic diagram of a pressure sensor under uniform normal pressure. (B) Strain distributions at the top, middle and bottom surface of the PET for the reference case in the x-direction. Strain distributions at the (C) top and (D) bottom surface of the PET for the hypothetical case of zero Poisson's ratio for the PDMS and skin.

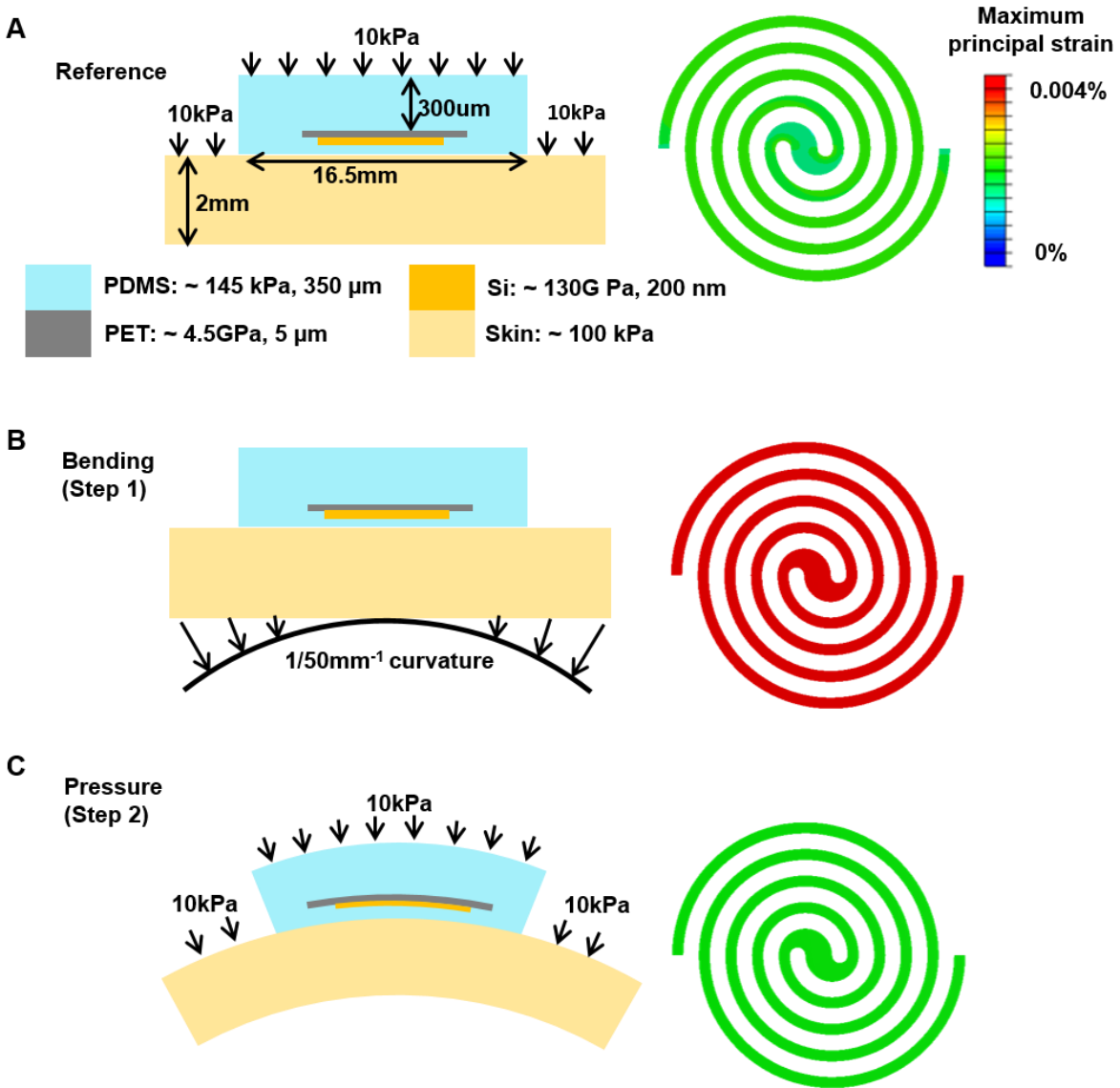


Fig. S6. Effect of bending on the pressure sensor. (A) A reference state of 10 kPa pressure applied to a flat device and skin. (B) Flat skin is bent onto a cylinder with $1/50\text{mm}^{-1}$ curvature. (C) 10 kPa pressure is applied after (B).

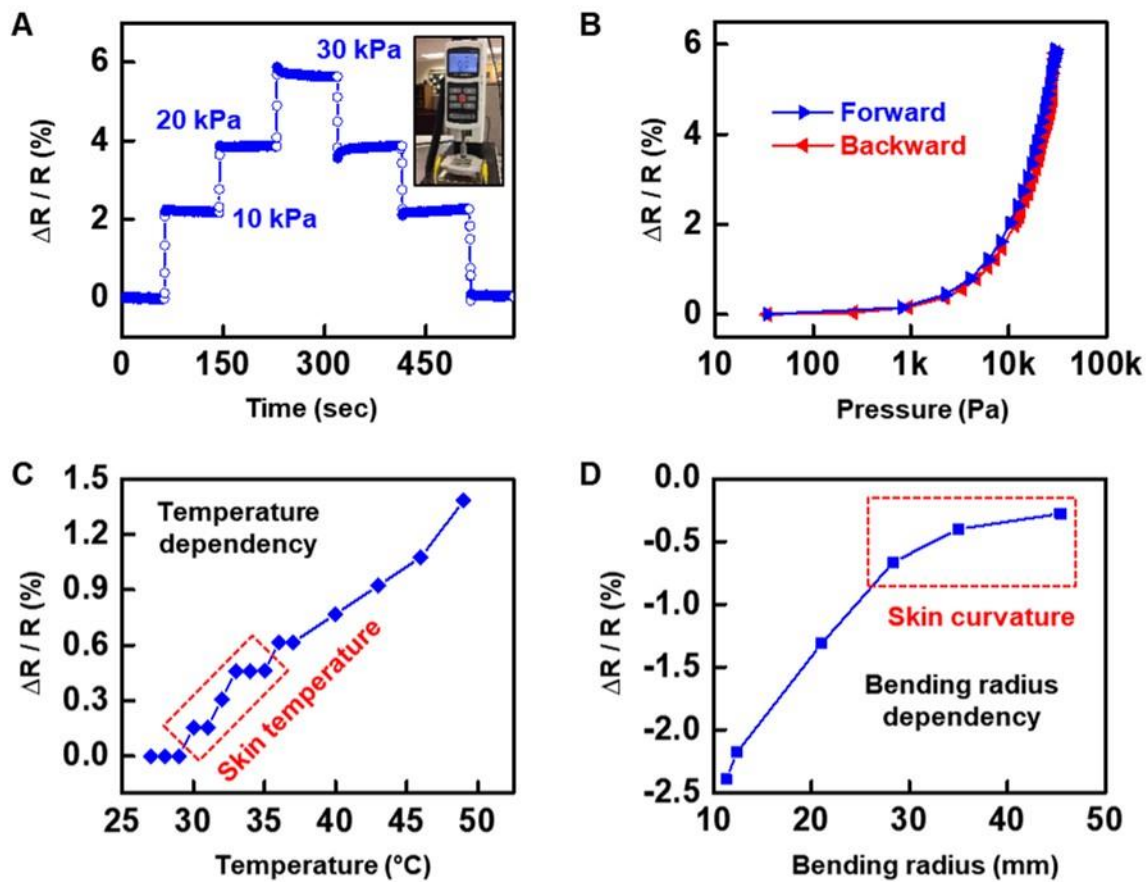


Fig. S7. Characterization of the boron-doped silicon pressure module. (A) Resistance change of the silicon membrane under various forms of pressure. (B) Resistance change as an applied pressure increases from 0 kPa to 30 kPa followed by release. (C) Data on the temperature dependence of the resistance of the silicon membrane. The red dotted box indicates a range typical for human skin. (D) Data on the bending dependence of the resistance of the silicon membrane, including values typical of human skin (red box).

| ams SL13A Demo | |
|-------------------------|------------------|
| UID: | e03605360052c168 |
| Temperature: | 32.2 °C |
| Battery Voltage: | N/A |
| Logging Form: | Dense |
| Storage Rule: | Normal |
| Interval: | 1 |
| Sensor: | Temperature |
| Battery Check: | Disabled |
| Extreme Upper Limit: | 0 |
| Upper Limit: | 0 |
| Lower Limit: | 0 |
| Extreme Lower Limit: | 0 |
| Measurement Status: | inactive |
| Number of Measurements: | 0 |

Fig. S8. Screen view of temperature monitoring with a smartphone application in real time.

The red box indicates the measured temperature of the skin: 32.2°C.

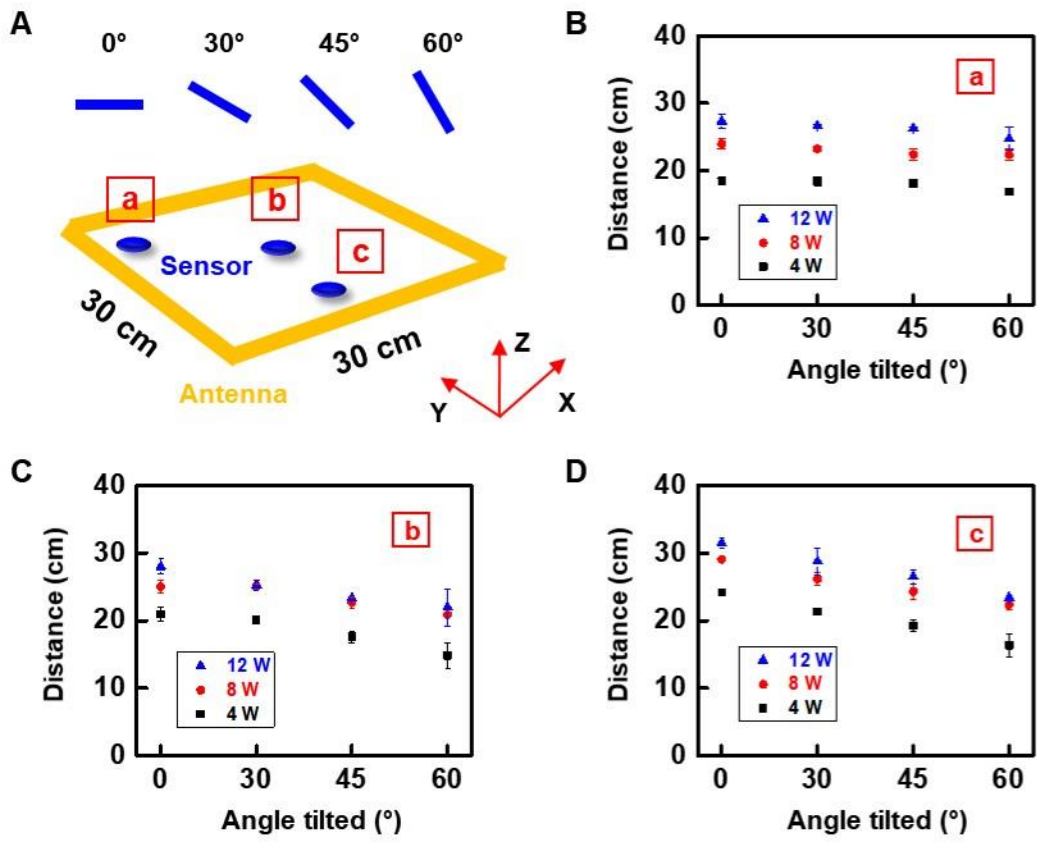


Fig. S9. Measurements of the effect of orientation under three power settings and representative positions. (A) Schematic illustration of the experiment setup. Results for the maximum operating range for three values of RF power to the antenna (4, 8, and 12 W) and representative positions (B) edge a (C) center b (D) and corner c.

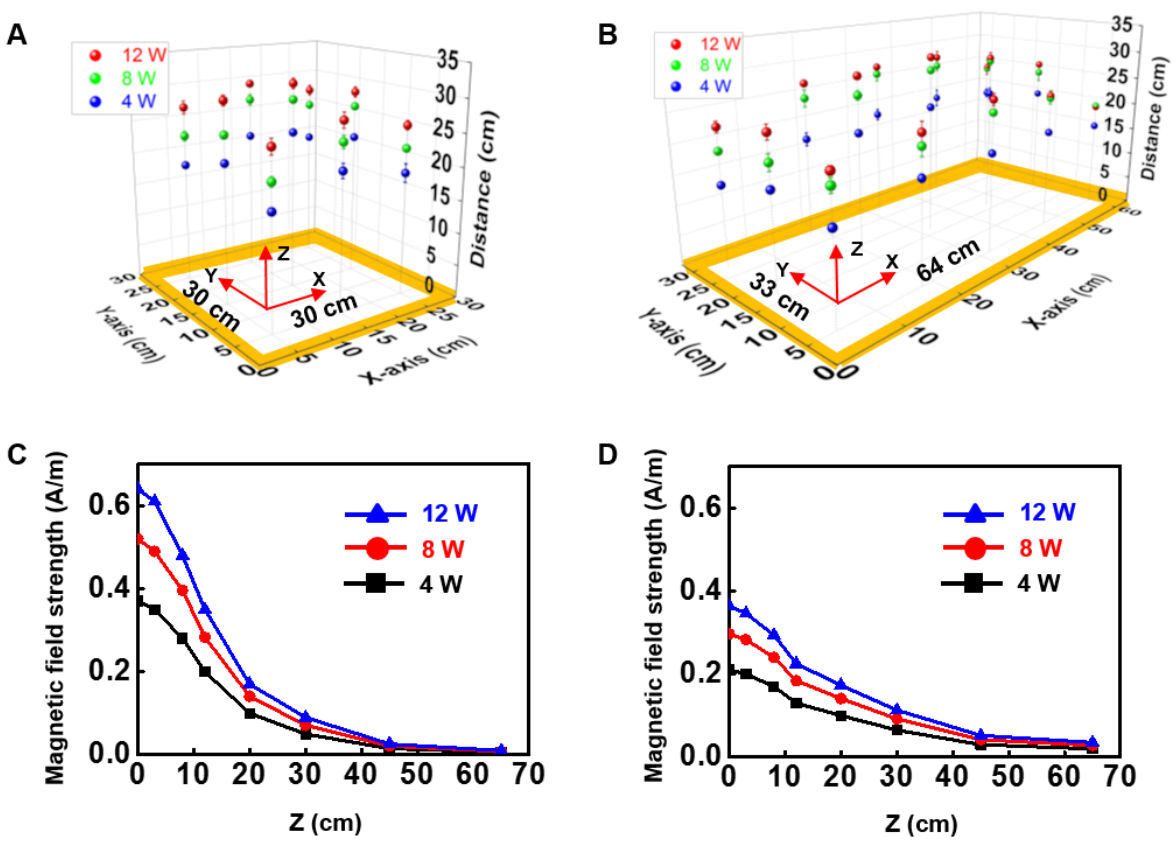


Fig. S10. Measurements of operating distance for sensors placed at various locations inside each antenna with different power levels. Transmission distances for HF loop antennas with sizes of (A) 300 mm x 300 mm x 40 mm and (B) 330 mm x 640 mm x 40 mm at various powers. Magnetic field strength determined by FEA for (C) 300 mm x 300 mm x 40 mm, (D) 330 mm x 640 mm x 40 mm HF loop antennas as a function of position along the z direction.

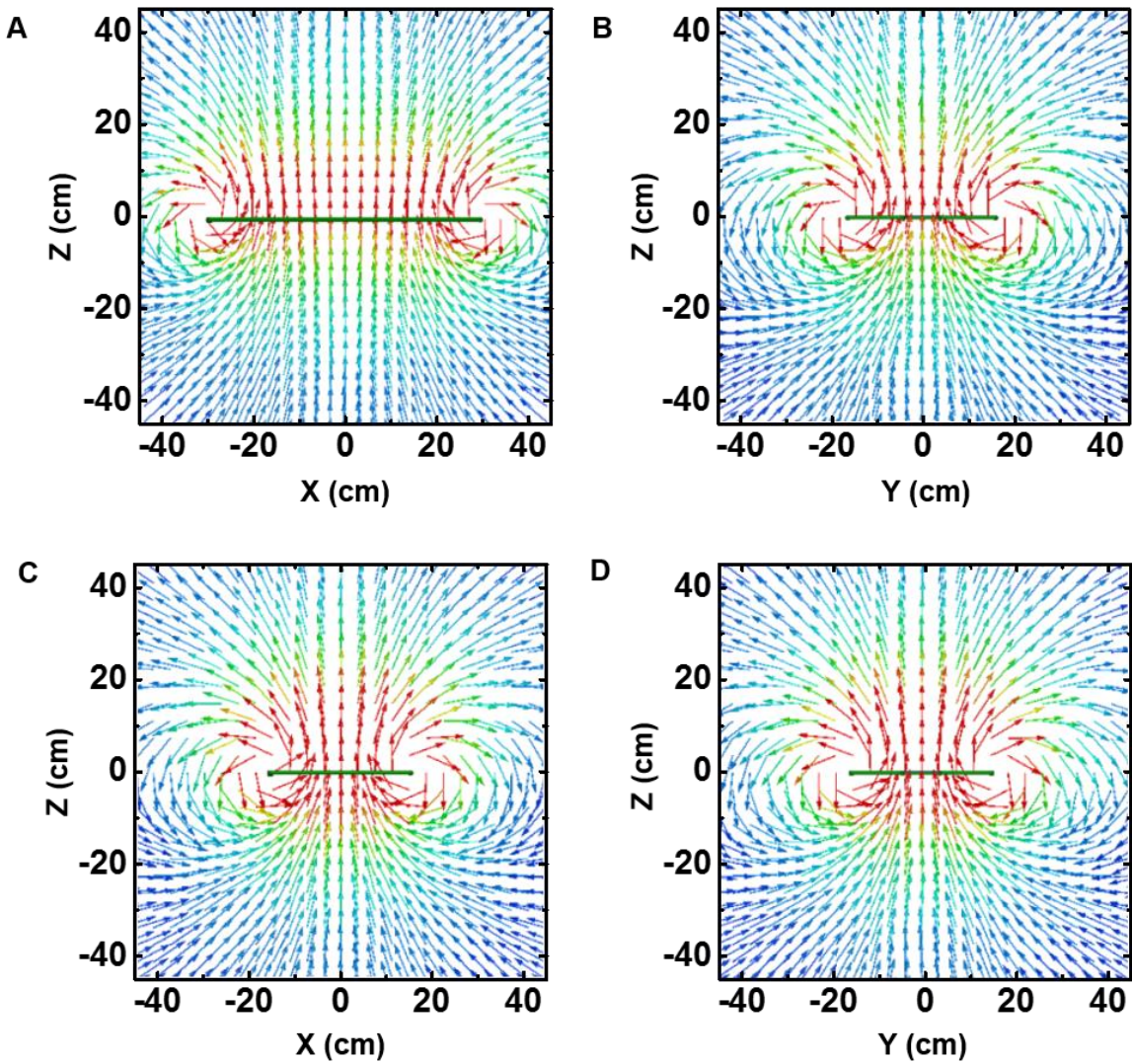


Fig. S11. Distributions of the magnetic field along the vertical direction for constant power (12 W) and different antenna sizes. (A-B) Computed magnetic field strength as a function of vertical distance (z) away from the x - y - z plane at various RF powers for medium (649 mm x 165 mm x 10 mm) and **(C-D)** small (300 mm x 300 mm x 10 mm) antennas.

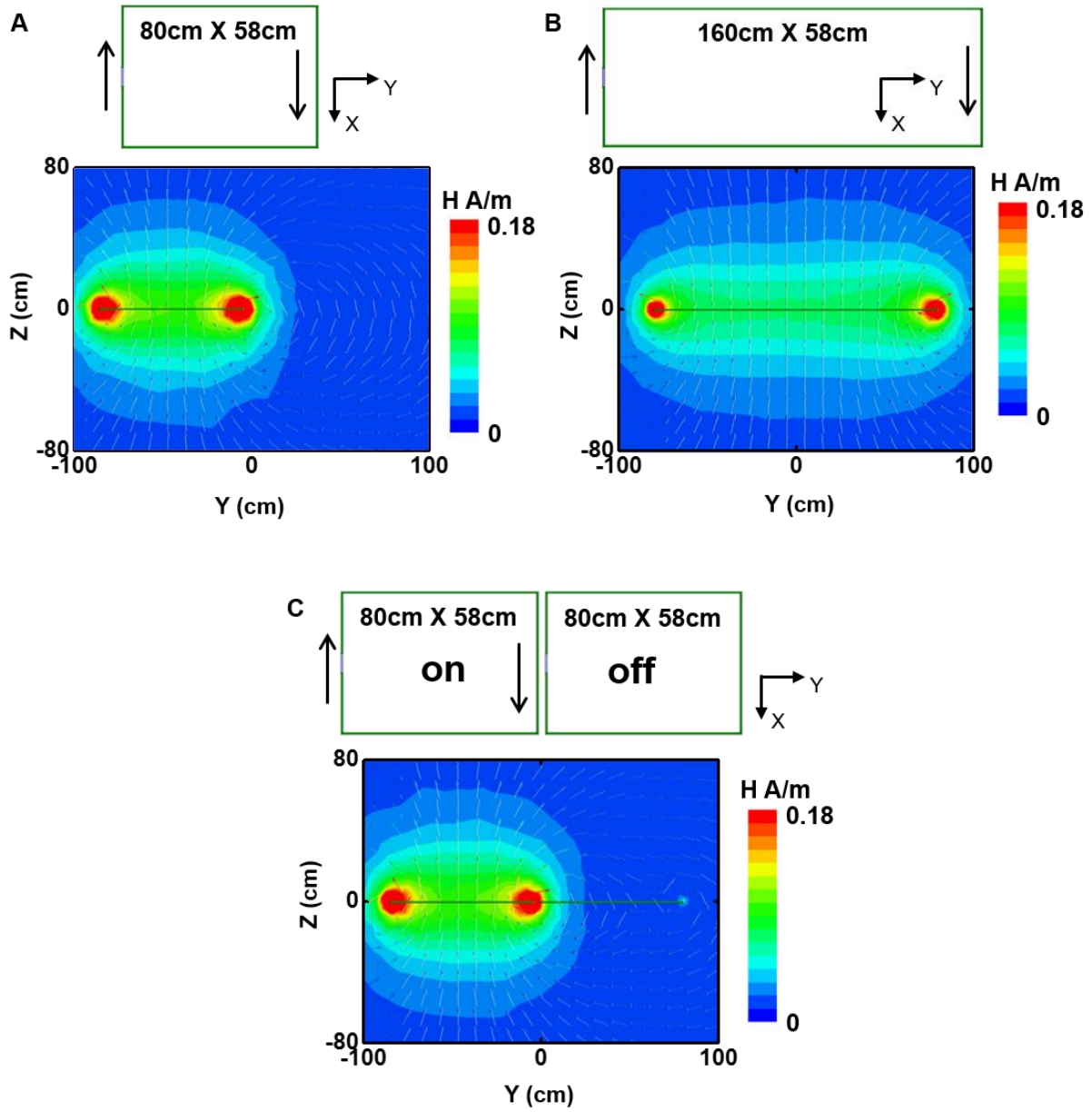


Fig. S12. Simulation of field strength of different antenna sizes and multiplexed operation.
 (A-B) Field strength for different antenna sizes; (C) field strength for multiplexed operation.

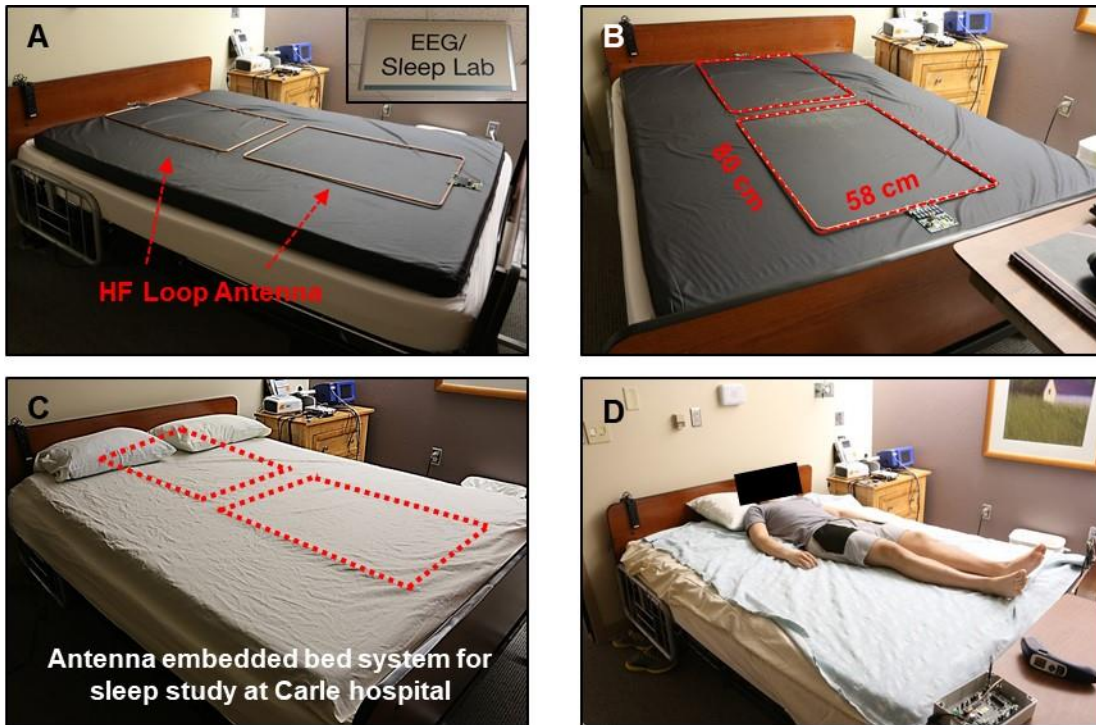


Fig. S13. Embedded antenna setup for sleep studies at Carle Hospital. (A-C) Images of a mattress embedded with two custom antennas for full-body coverage. (D) Image of a participant with 65 NFC temperature sensors lying on the mattress for the sleep study.

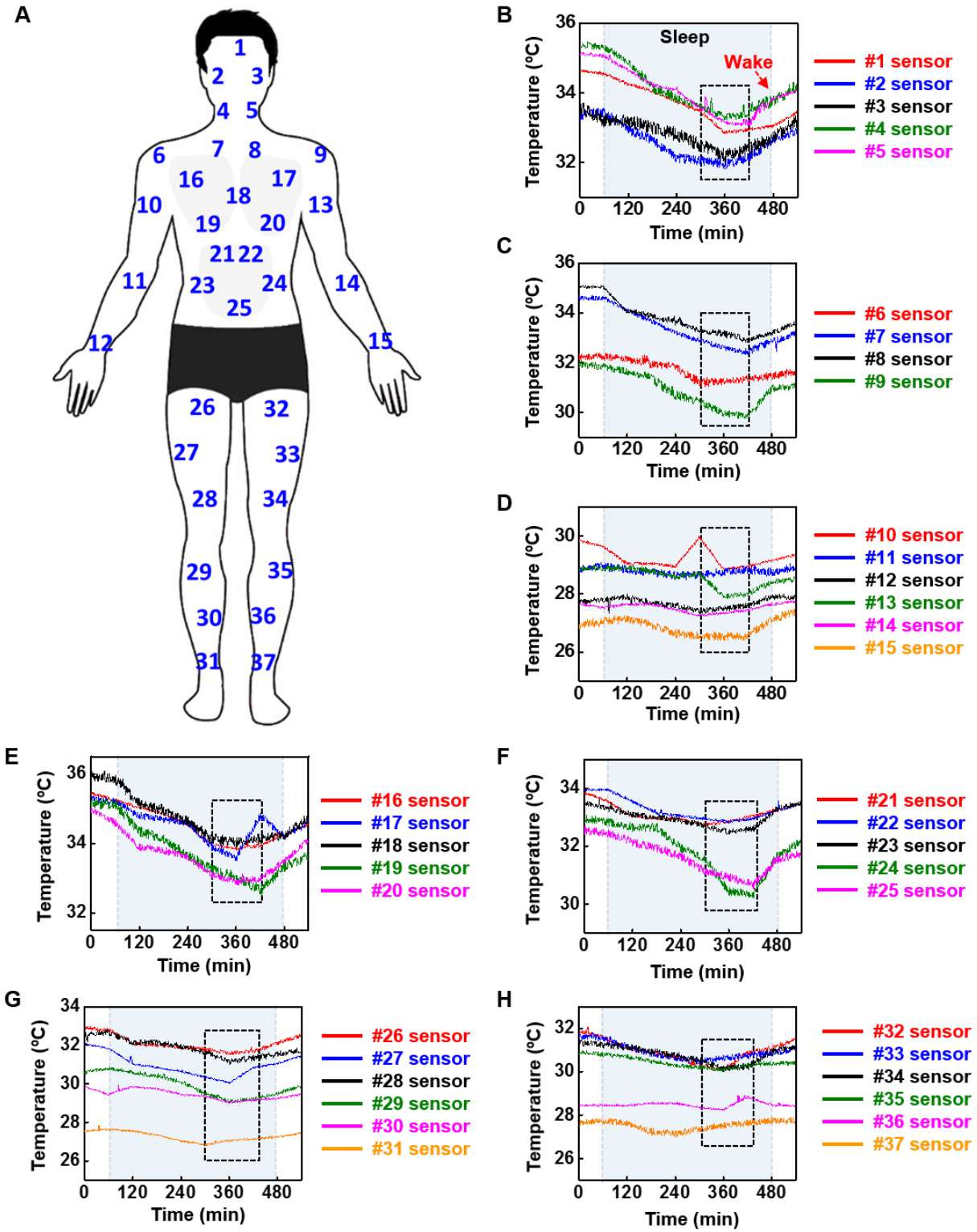


Fig. S14. Results of sleep studies conducted with arrays of temperature sensors on the front of the body. (A) Schematic illustration of the locations of 37 temperature sensors on the front

side of the body. **(B-H)** Temperature measurements during a 9-hour sleep study. The blue highlighted region indicates the period of sleep. The black box indicates the time period of minimum body temperature, which occurs at 2~3 hours before waking up.

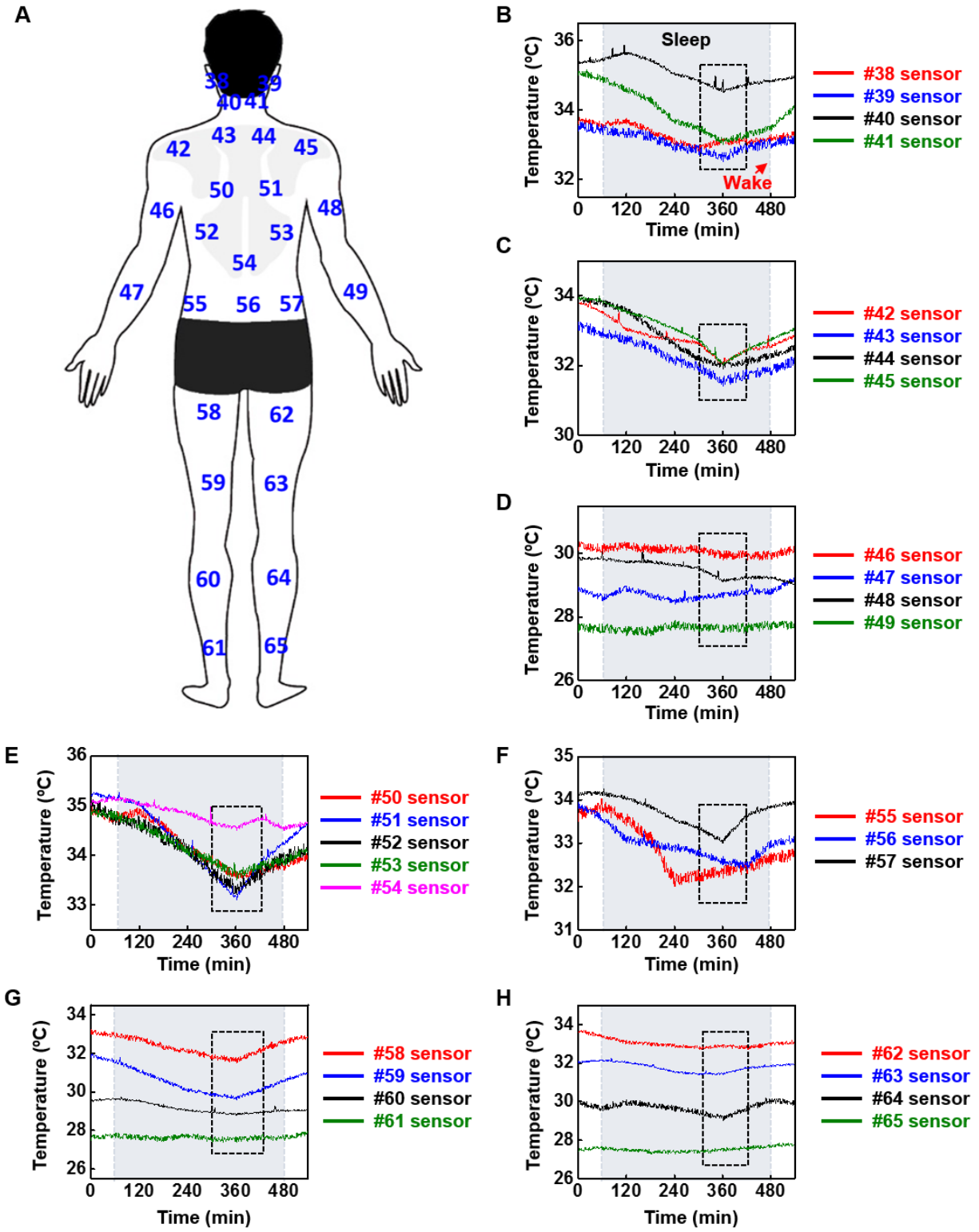


Fig. S15. Results of sleep studies conducted with arrays of temperature sensors on the back of the body. (A) Schematic illustration of the locations of 28 temperature sensors on the front

side of the body (**B-H**) Temperature measurements during a 9-hour sleep study. The blue highlighted region indicates the period of sleep.

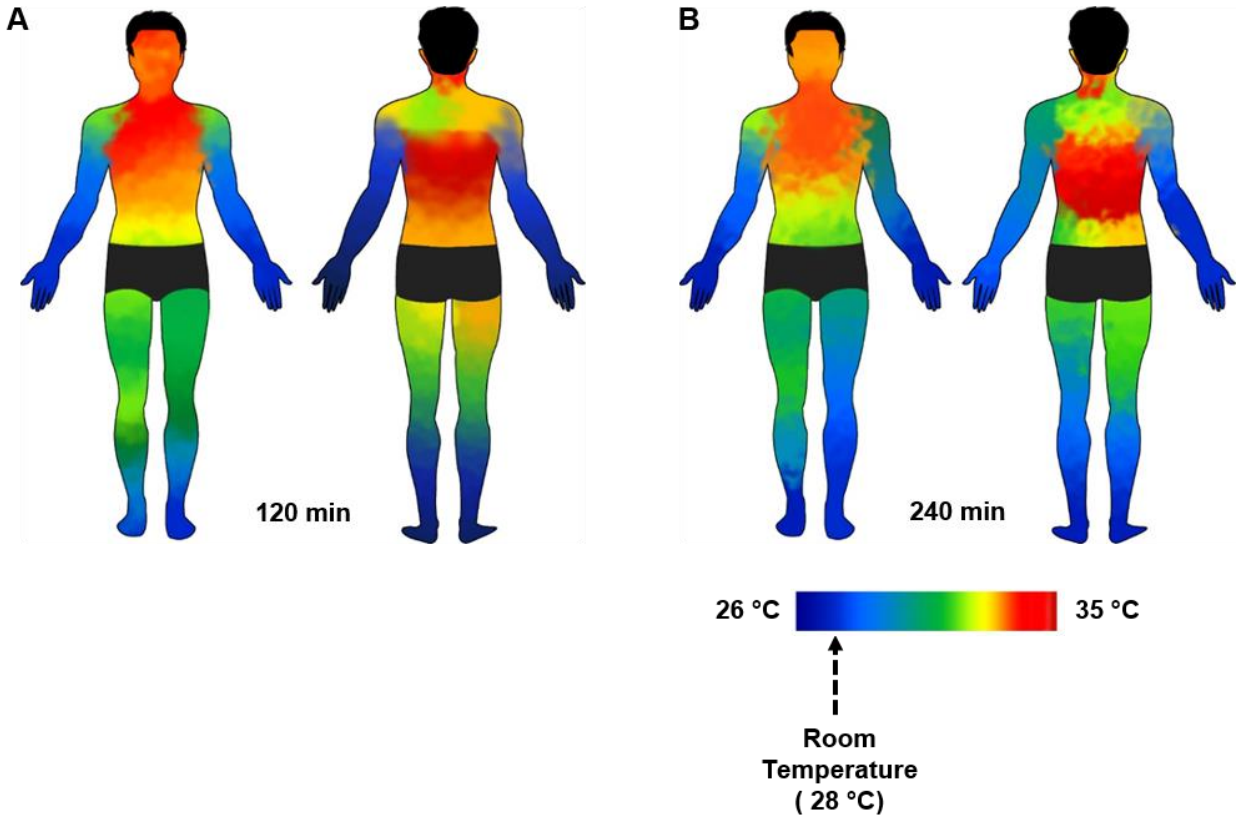


Fig. S16. Color heat maps of the entire body constructed from temperature data collected using NFC sensors. Full body heat color maps (A) 1 hour and (B) 3 hours after falling asleep.

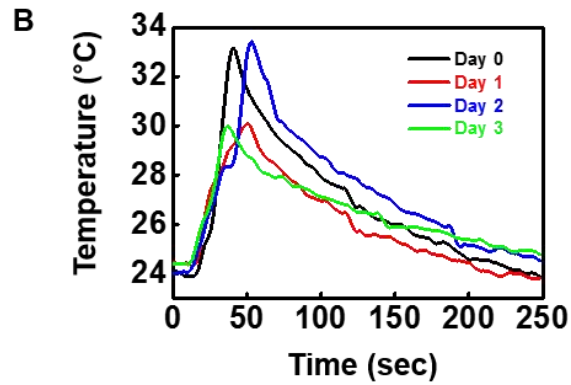


Fig. S17. Results of the sensors' lifetime during 3 days of continuous wear. (A) Optical images of the NFC sensor on a healthy human's back each day. **(B)** Graph of temperature recorded using the adhered NFC sensor daily.

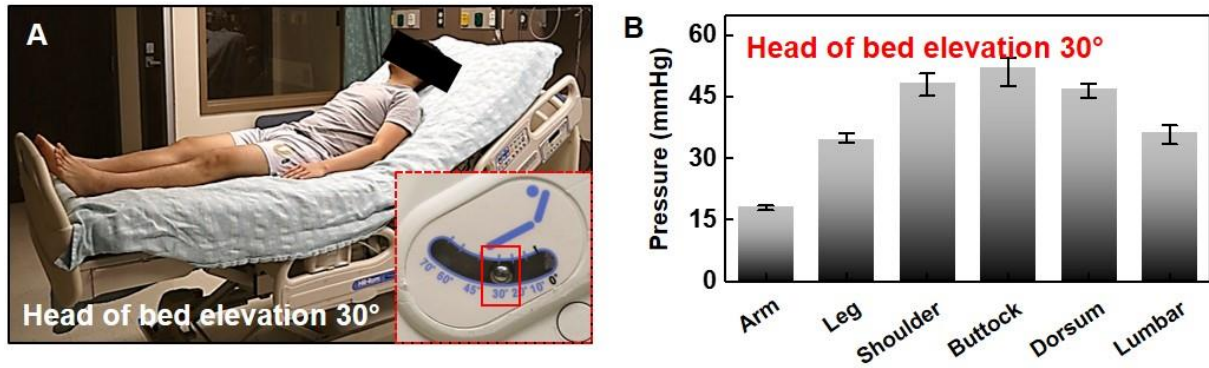
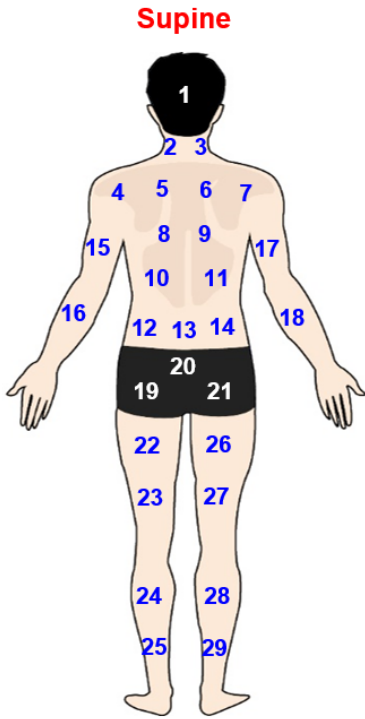
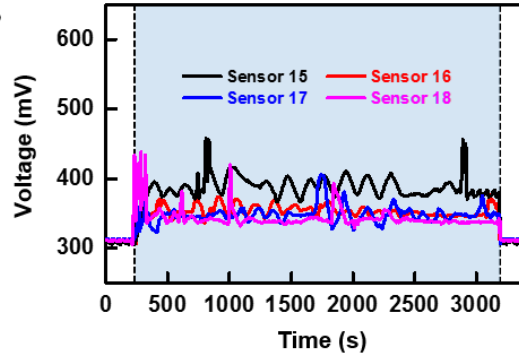


Fig. S18. Results of wirelessly recorded data obtained while lying at a supine angle of 30°. Red box highlights supine angle. **(A)** Photograph of the subject lying on the hospital bed. **(B)** Result of the pressure recorded at each body position (the number of sensors for average, arm: 4, leg: 4, shoulder: 4, buttock: 3, dorsum: 4, lumbar: 3, error bar: standard deviation, 1 set).

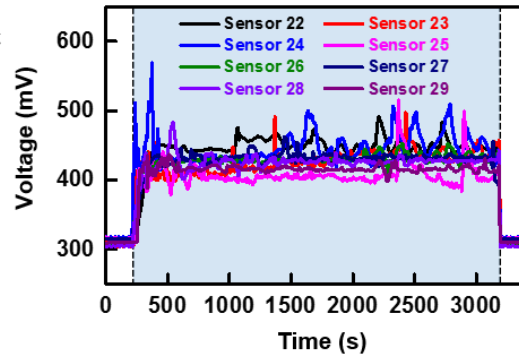
A



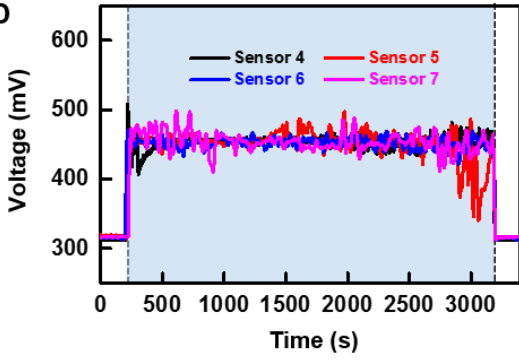
B



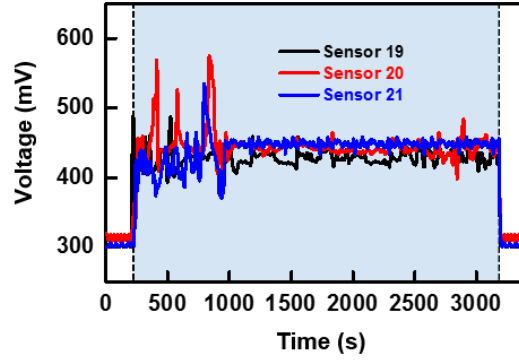
C



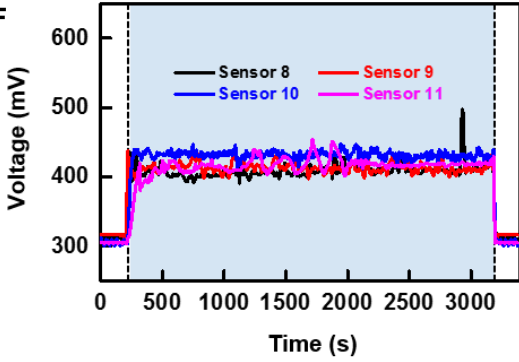
D



E



F



G

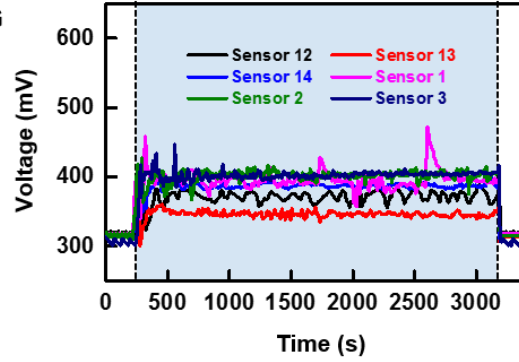


Fig. S19. Graphs of pressure measurements in a hospital bed while lying at a supine angle of 0° (data with individual sensor). (A) Schematic illustration of the position of the 29 NFC pressure sensors across the (B) arm, 15~18 (C) leg, 22~29 (D) shoulder, 4~7 (E) buttock, 19~21 (F) dorsum, 8~11 (G) lumbar, 12~14; head, 1; neck, 2~3.

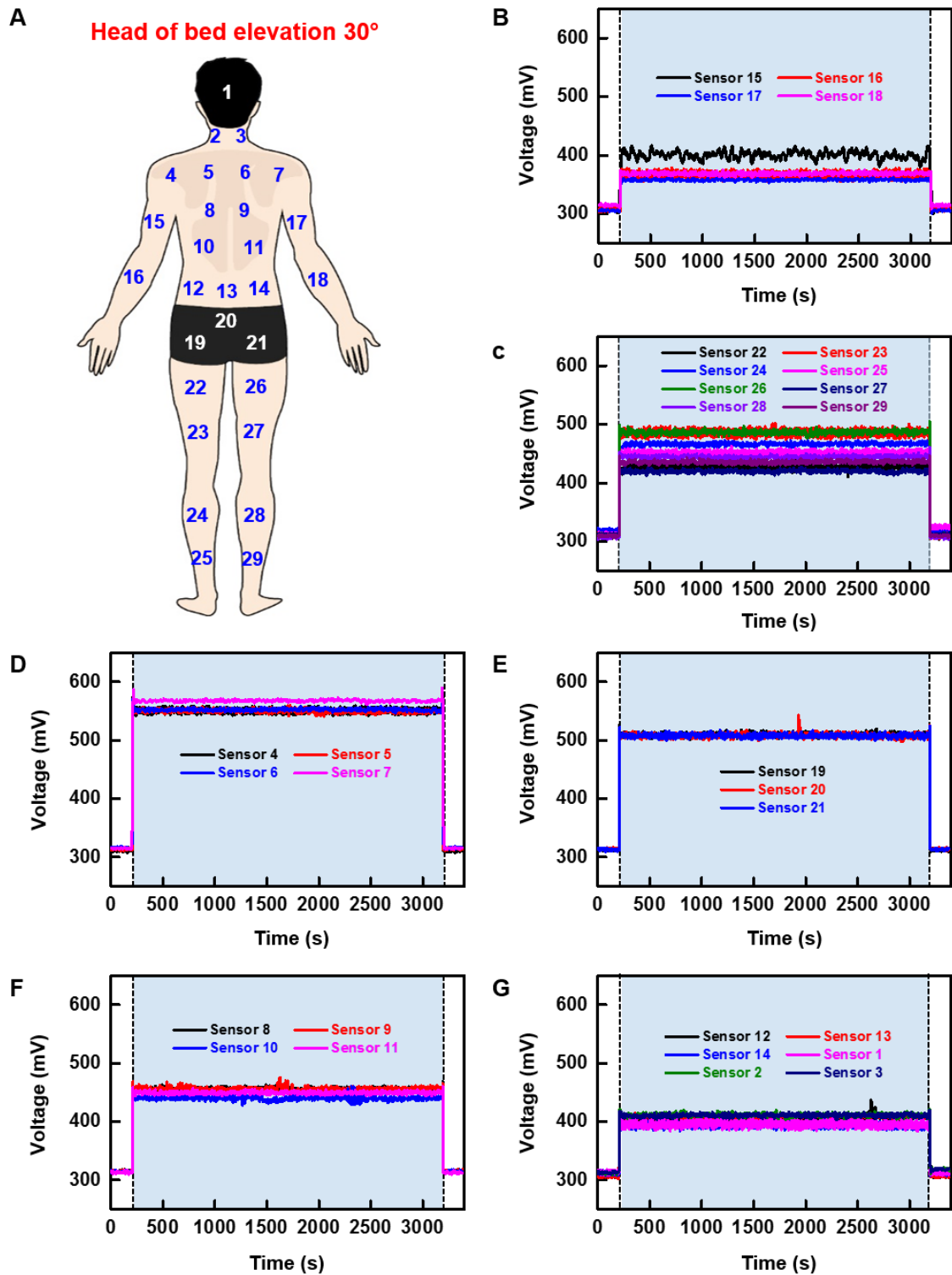


Fig. S20. Graphs of pressure measurements obtained in a hospital bed while lying at a supine angle of 30° (data with individual sensor). (A) Schematics illustration of the position of

the 29 NFC pressure sensors across the **(B)** arm, 15~18 **(C)** leg, 22~29 **(D)** shoulder, 4~7 **(E)** buttock, 19~21 **(F)** dorsum, 8~11 **(G)** lumbar, 12~14; head, 1; neck, 2~3.

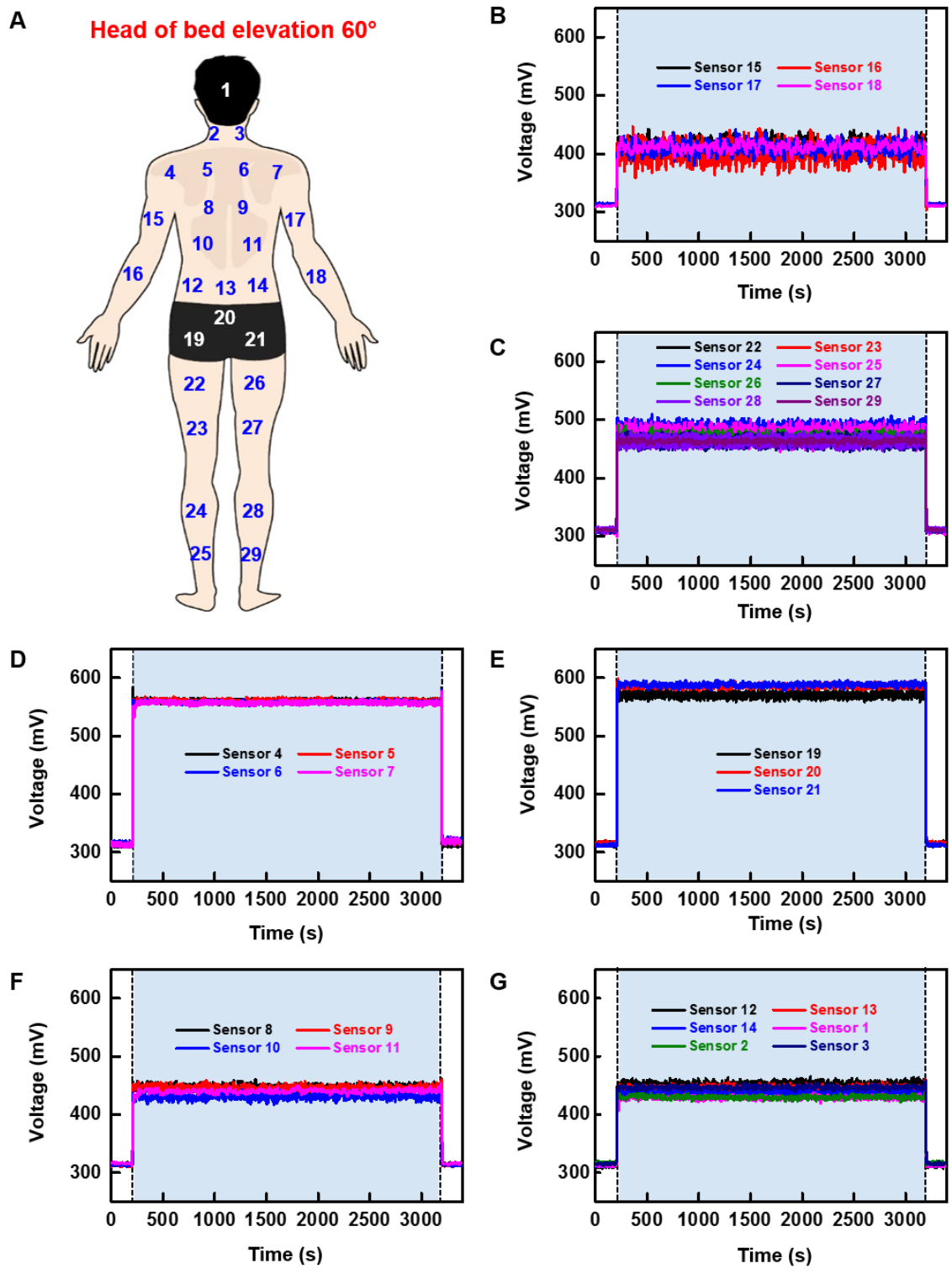


Fig. S21. Graphs of pressure measurements obtained in a hospital bed while lying at a supine angle of 60° (data with individual sensor). (A) Schematics illustration of the position of

the 29 NFC pressure sensors across the **(B)** arm, 15~18 **(C)** leg, 22~29 **(D)** shoulder, 4~7 **(E)** buttock, 19~21 **(F)** dorsum, 8~11 **(G)** lumbar, 12~14; head, 1; neck, 2~3.

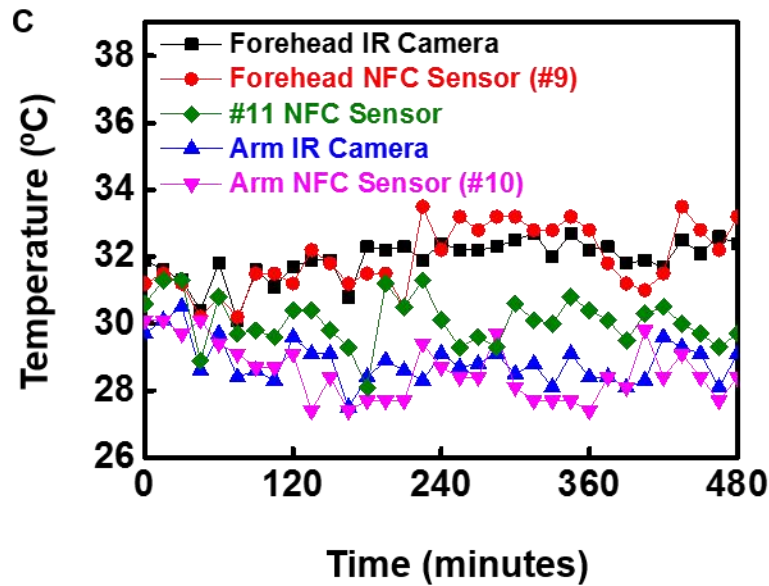
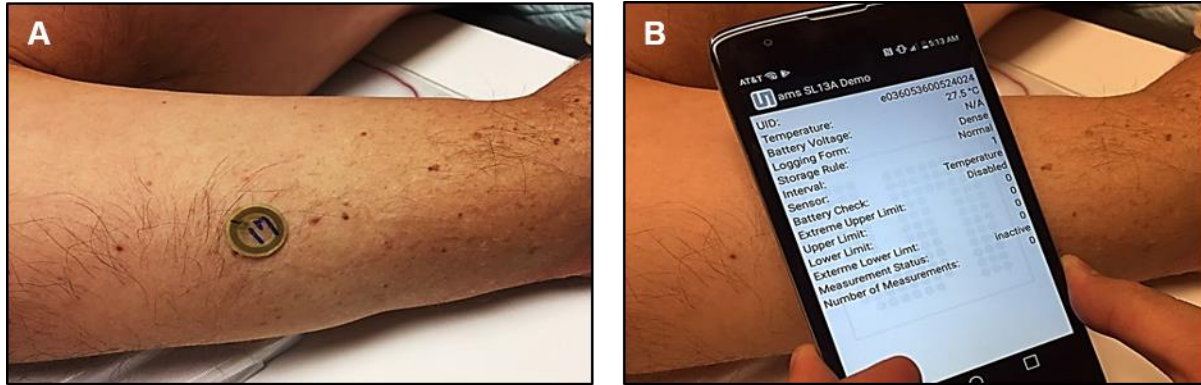


Fig. S22. Summary of comparative studies of temperature measurements in a clinical sleep laboratory: first night. (A) Picture of the subject's limb with a wireless sensor attached on the upper arm. (B) Picture of the process of wireless measurement of limb temperature using a smartphone. (C) Temperature of the forehead and the upper bicep regions captured using wireless sensors and IR thermography (data with individual sensor).

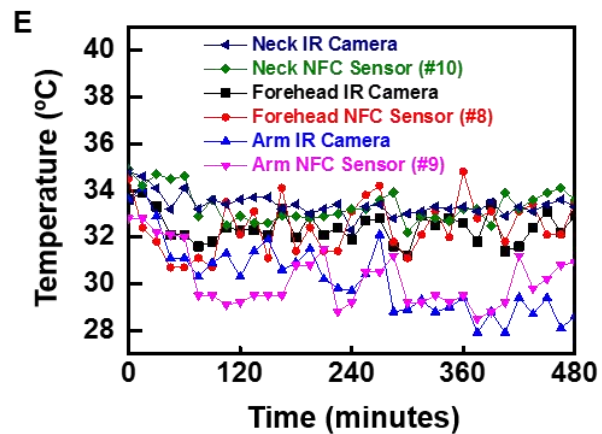
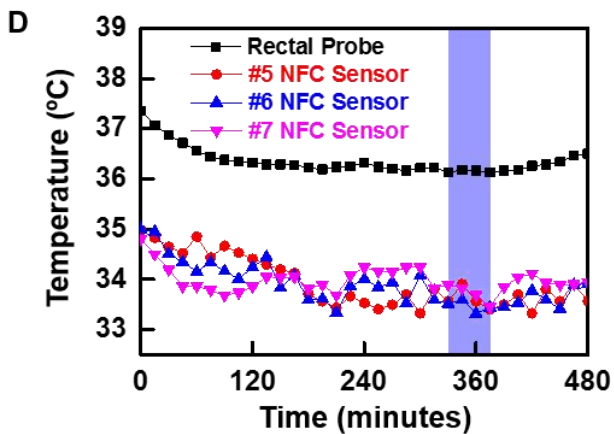
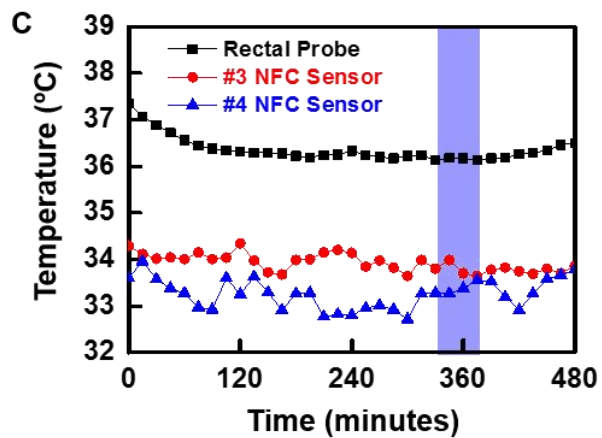
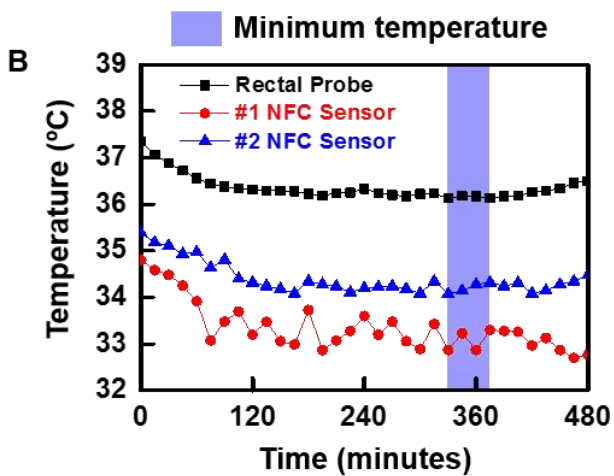
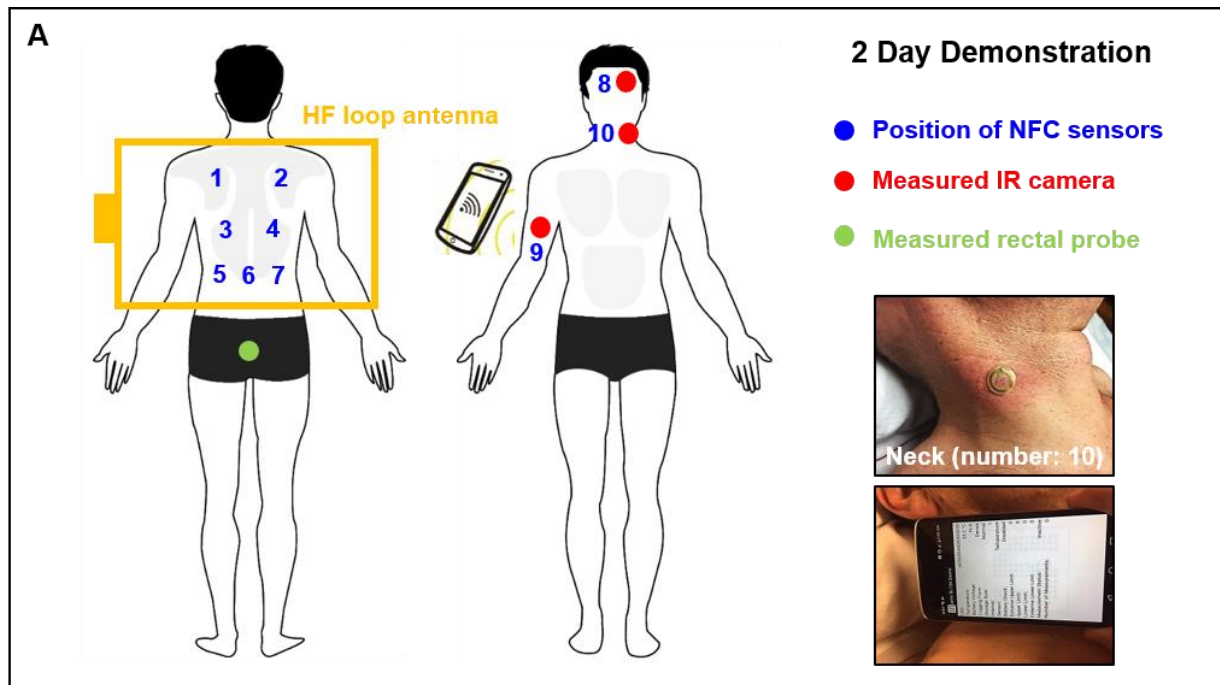
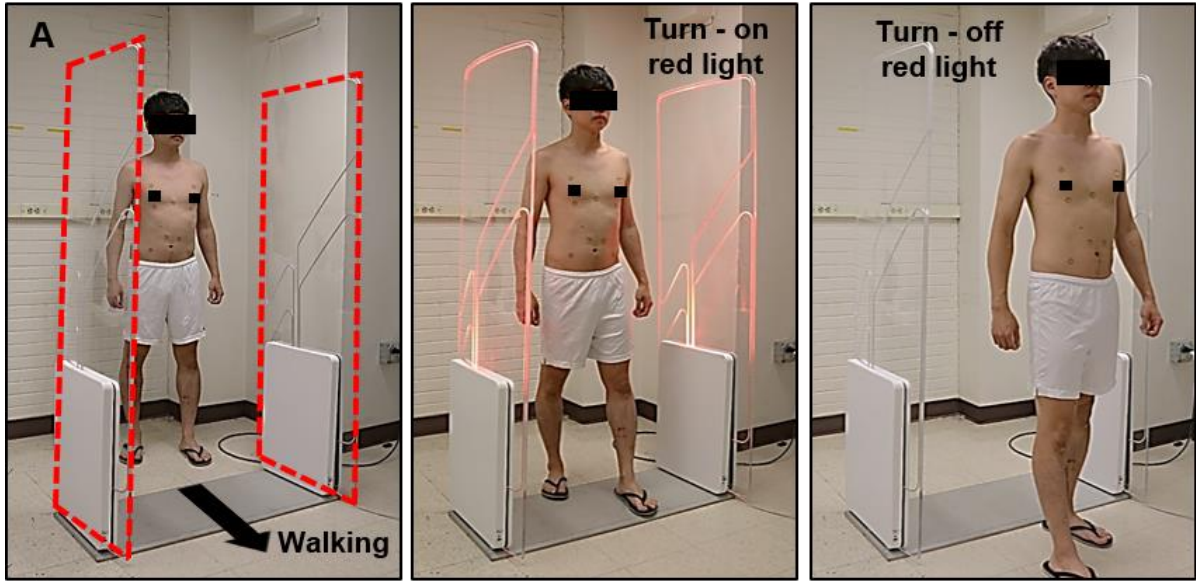


Fig. S23. Summary of the experimental setup and data collected in comparative studies of temperature measurements in a clinical sleep laboratory: second night. (A) Schematic illustration of the locations for temperature measurement using wireless sensors, IR camera, and rectal probe. (B) Temperature in the shoulder region captured using wireless sensors. (C, D) Temperature in the thoracic and lumbar regions captured using wireless sensors. (E) Temperature of the forehead, the neck and the upper bicep regions captured using wireless sensors and IR thermography.



Gate size of full-body covered HF loop antenna

B

Number of NFC temperature sensors

| No. | Tag-Name | Serial Number | DSFRID |
|-----|-----------------------------|------------------|--------|
| 1 | ISO15693 - IDS Microchip AG | 6036053600524021 | 00 |
| 2 | ISO15693 - IDS Microchip AG | 603605360048C2F5 | 00 |
| 3 | ISO15693 - IDS Microchip AG | 6036053600550187 | 00 |
| 4 | ISO15693 - IDS Microchip AG | 603605360048C2E8 | 00 |
| 5 | ISO15693 - IDS Microchip AG | 6036053600500380 | 00 |
| 6 | ISO15693 - IDS Microchip AG | 603605360048C2FD | 00 |
| 7 | ISO15693 - IDS Microchip AG | 6036053600500314 | 00 |
| 8 | ISO15693 - IDS Microchip AG | 6036053600524024 | 00 |
| 9 | ISO15693 - IDS Microchip AG | 603605360048E290 | 00 |
| 10 | ISO15693 - IDS Microchip AG | 6036053600548100 | 00 |
| 11 | ISO15693 - IDS Microchip AG | 6036053600502200 | 00 |
| 12 | ISO15693 - IDS Microchip AG | 603605360048C300 | 00 |
| 13 | ISO15693 - IDS Microchip AG | 603605360048C301 | 00 |
| 14 | ISO15693 - IDS Microchip AG | 6036053600505180 | 00 |
| 15 | ISO15693 - IDS Microchip AG | 60360536005280E0 | 00 |
| 16 | ISO15693 - IDS Microchip AG | 603605360048C2F1 | 00 |
| 17 | ISO15693 - IDS Microchip AG | 603605360052C100 | 00 |
| 18 | ISO15693 - IDS Microchip AG | 603605360048E28E | 00 |
| 19 | ISO15693 - IDS Microchip AG | 603605360048C2E8 | 00 |
| 20 | ISO15693 - IDS Microchip AG | 603605360048C2F2 | 00 |
| 21 | ISO15693 - IDS Microchip AG | 60360536005051C0 | 00 |
| 22 | ISO15693 - IDS Microchip AG | 603605360052C104 | 00 |
| 23 | ISO15693 - IDS Microchip AG | 603605360052C106 | 00 |
| 24 | ISO15693 - IDS Microchip AG | 603605360048C2D6 | 00 |
| 25 | ISO15693 - IDS Microchip AG | 60360536005280E0 | 00 |
| 26 | ISO15693 - IDS Microchip AG | 6036053600500200 | 00 |
| 27 | ISO15693 - IDS Microchip AG | 603605360052C169 | 00 |
| 28 | ISO15693 - IDS Microchip AG | 60360536005501C0 | 00 |
| 29 | ISO15693 - IDS Microchip AG | 60360536005280ED | 00 |
| 30 | ISO15693 - IDS Microchip AG | 603605360052C0F0 | 00 |
| 31 | ISO15693 - IDS Microchip AG | 603605360048C30A | 00 |
| 32 | ISO15693 - IDS Microchip AG | 603605360050038A | 00 |
| 33 | ISO15693 - IDS Microchip AG | 603605360048E29F | 00 |
| 34 | ISO15693 - IDS Microchip AG | 603605360054C1A0 | 00 |
| 35 | ISO15693 - IDS Microchip AG | 60360536005501C0 | 00 |
| 36 | ISO15693 - IDS Microchip AG | 60360536005280EA | 00 |
| 37 | ISO15693 - IDS Microchip AG | 603605360048A1FA | 00 |
| 38 | ISO15693 - IDS Microchip AG | 603605360054C1A0 | 00 |
| 39 | ISO15693 - IDS Microchip AG | 603605360048C2D0 | 00 |
| 40 | ISO15693 - IDS Microchip AG | 603605360052C100 | 00 |
| 41 | ISO15693 - IDS Microchip AG | 60360536005001B0 | 00 |
| 42 | ISO15693 - IDS Microchip AG | 603605360048E29F | 00 |
| 43 | ISO15693 - IDS Microchip AG | 60360536005501C0 | 00 |
| 44 | ISO15693 - IDS Microchip AG | 60360536005501C0 | 00 |
| 45 | ISO15693 - IDS Microchip AG | 60360536005480E0 | 00 |

Serial number of NFC chip

Fig. S24. Demonstration of a gate-type reader system and antenna. (A) Picture of human subject with 45 sensors walking through a gate-sized HF loop antenna with associated reader electronics. The red light indicates that the system is successfully communicating with the sensors. (B) Summary of data that illustrates recognition of all 45 sensors and their unique serial numbers.

Maximum principal strain at the top of Si membrane

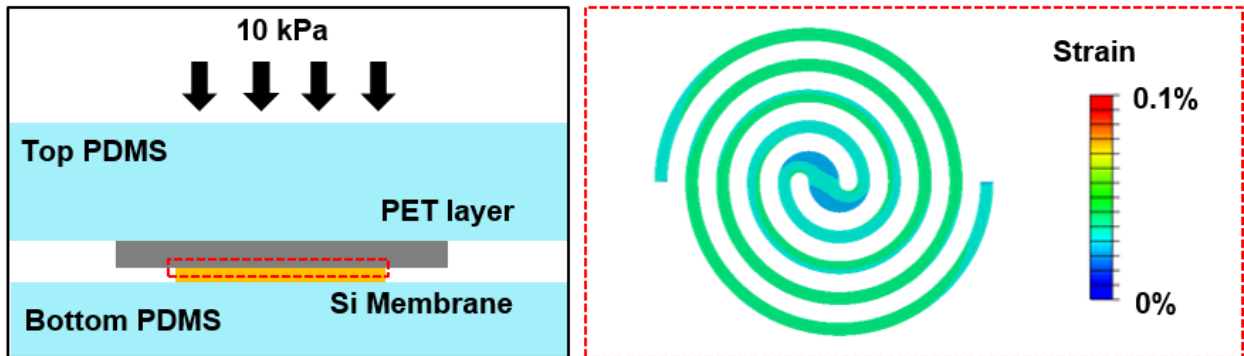


Fig. S25. Strain distributions at the silicon layer induced by local pressure. Computations for an applied force of 10 kPa suggest a gauge factor of ~ 50 .

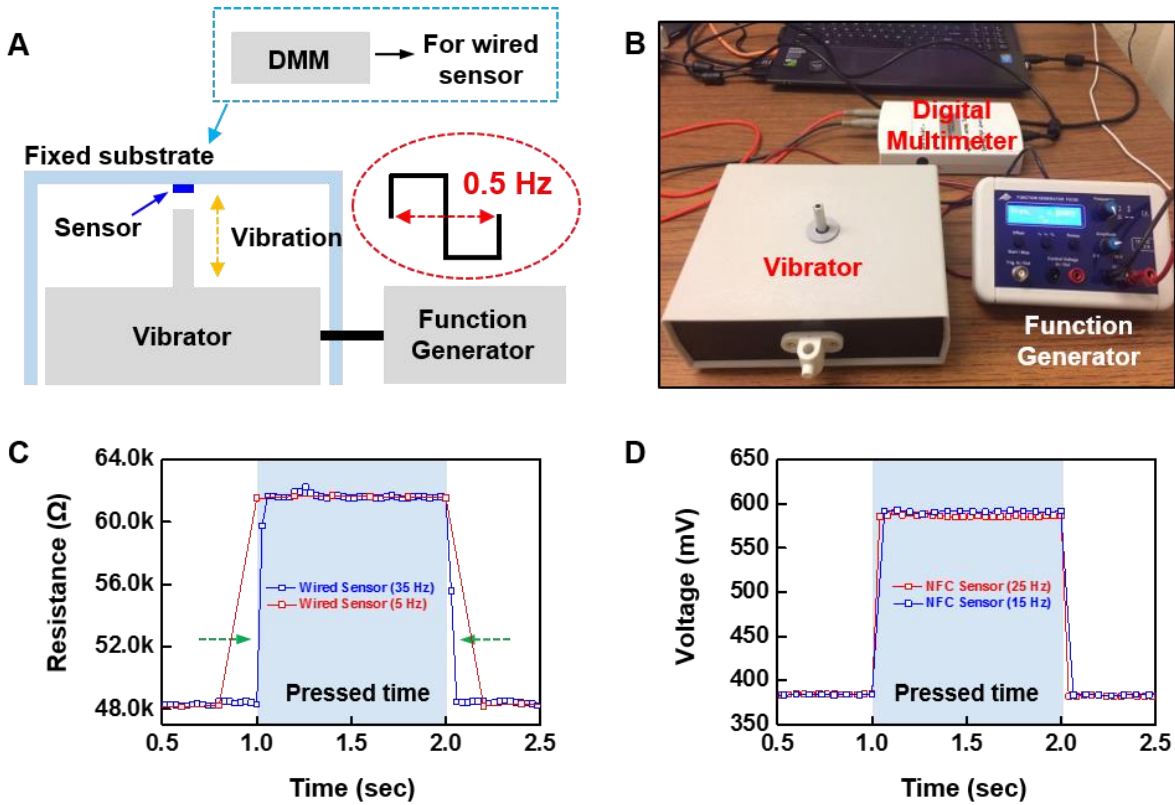


Fig. S26. Measurements of response time obtained using a vibrating actuator stage and a function generator. (A) Schematic illustration of the placement of wireless and wired pressure sensors under a vibrating actuator tip. **(B)** Image of the experimental equipment. **(C-D)** Results of the response time experiment (blue shaded area: pressed time).

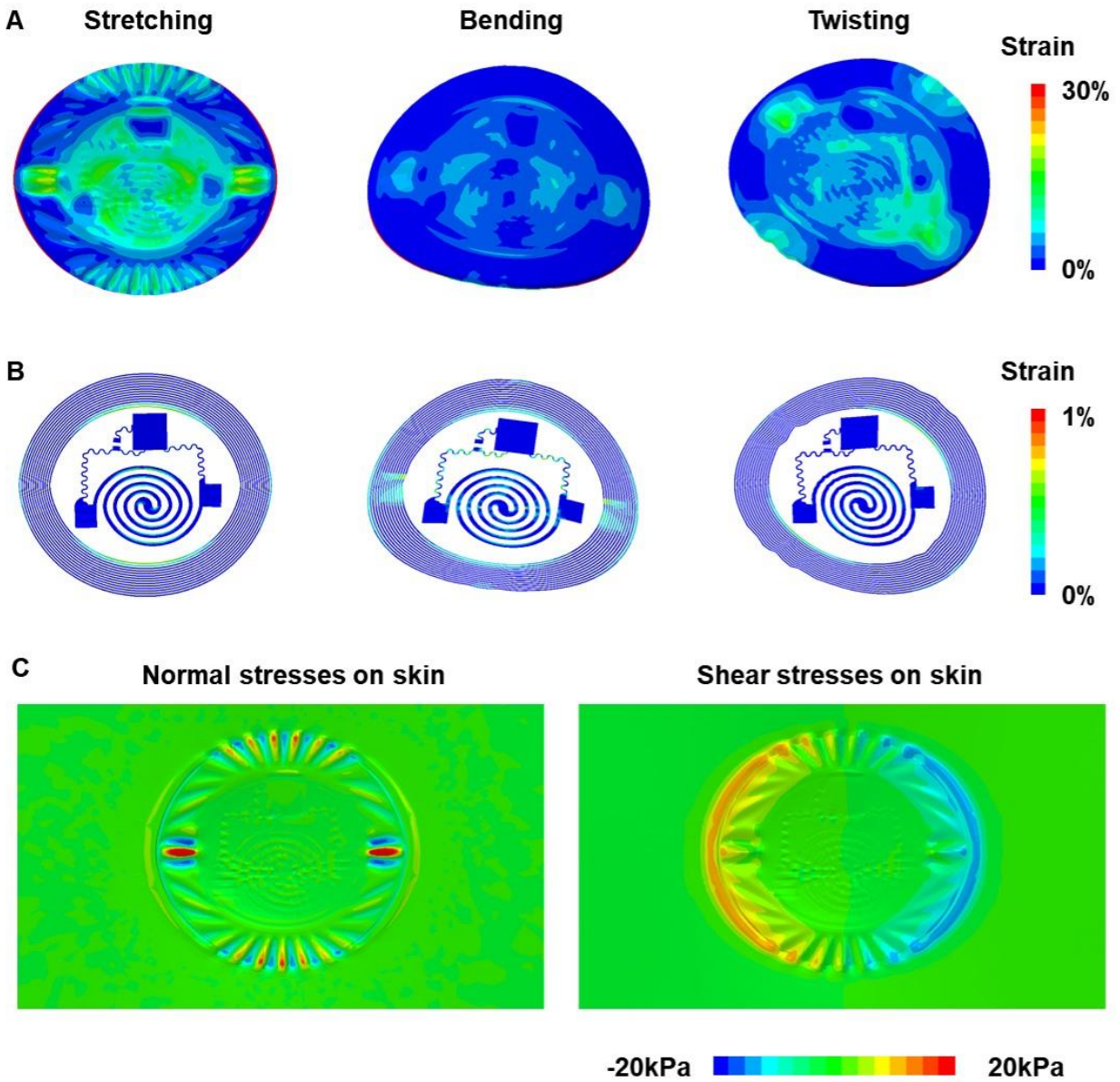


Fig. S27. Mechanical response of an encapsulated sensor on a phantom skin under stretching, bending, and twisting. Strain distributions (A) at the top PDMS and (B) at the copper and silicon layers. (C) Interfacial stresses between an encapsulated NFC device and phantom skin with normal stresses and shear stresses.

SUPPLEMENTARY VIDEOS

Movie S1. Recordings from a single sensor captured using NFC between an epidermal device and a smartphone through a prosthetic.

Movie S2. Recordings from four sensors simultaneously using a large-scale (800 mm × 580 mm × 400 mm) RF antenna through a prosthetic.